TECNOLOGIA SETÚBAL
ESCOLA SUPERIOR · POLITÉCNICO SETÚBAL

SAÚDE
ESCOLA SUPERIOR · POLITÉCNICO SETÚBAL

Miguel Ângelo
Valente Albardeiro

Development by Robocasting of Scaffolds of HAp-ZnO and HAp-MgO composites for bone tissue regeneration

Thesis to obtain the Master of Science Degree in Biomedical Engineering

SUPERVISORS

PhD Professor Célio Pina

PhD Professor Ricardo Baptista

December 2024

PRR Plano de Recuperação e Resiliência
REPÚBLICA PORTUGUESA
Financiado pela União Europeia
NextGenerationEU

Miguel Ângelo
Valente Albardeiro

Development by Robocasting of Scaffolds of HAp-ZnO and HAp-MgO composites for bone tissue regeneration

Examination Committee

Chairperson: PhD Professor, Anna Luiza Barszczak Sardinha Letournel, Instituto Politécnico de Setúbal

Supervisor: PhD Professor, Célio Gabriel Figueiredo Pina, Instituto Politécnico de Setúbal

Member of the Committee: PhD Professor, Izabela-Cristina Stancu, National University of Science and Technology Politehnica of Bucharest

December 2024

Agradecimentos

Desde mais, gostaria de começar por expressar o meu agradecimento aos meus orientadores, por toda disponibilidade, conhecimento e força transmitida ao longo deste tempo. Ao Professor Célio Pina, pela disposição e conselhos, puxando sempre para cima de modo a atingir os meus objetivos. E ao Professor Ricardo Baptista, por toda a sua disponibilidade, independentemente de onde esteja e por todos os conselhos e ideias que me deu. Um obrigado aos dois.

Quero agradecer à Escola Superior de Tecnologia do Instituto Politécnico de Setúbal, pela oportunidade de frequentar este mestrado e por fornecer os recursos para a realização deste trabalho.

Ao Instituto Superior Técnico da Universidade de Lisboa, em especial ao grupo do CeFEMA, por fornecerem equipamentos e materiais para a realização deste trabalho.

Aos meus colegas e amigos de laboratório: Bruno, Marta, Daniel, Ruben, Beatriz e aos restantes. Por todos estes meses que passamos juntos e todos os bons e maus momentos, vocês estiveram sempre lá. Aos meus colegas de mestrado em especial à Rita, Inês, Adriana, Ângela e Sofia. Sem vocês o mestrado não tinha significado o mesmo, e principalmente por me aturarem.

À minha família. Obrigado por toda a força e apoio que me deram.
Em especial aos meus pais por todo o carinho e incentivo a querer sempre mais e explorar o que gosto. E à minha Avó, por tudo o que fez por mim.

E um obrigado a todas as pessoas que não mencionei, mas sabem o quão importantes são e me apoiarem a ser quem sou.

Resumo

As doenças e traumas ósseos afetam milhões de pessoas a nível global e, com o aumento da esperança média de vida, prevê-se que a sua prevalência continue a crescer. Os implantes metálicos representam o *golden standard* nos tratamentos atuais. No entanto, em casos mais graves, torna-se necessário recorrer a substitutos ósseos, como enxertos. Este tipo de abordagem enfrenta diversas limitações, incluindo disponibilidade reduzida, dimensões inadequadas e risco de rejeição imunológica. Neste contexto, a impressão 3D surge como uma solução inovadora, possibilitando a criação de enxertos sintéticos personalizados para cada paciente, utilizando materiais biocompatíveis que promovem a regeneração óssea, reduzindo complicações e acelerando a recuperação.

O objetivo deste estudo consiste no desenvolvimento de *scaffolds* compósitos à base de hidroxiapatite, incorporando óxido de zinco e óxido de magnésio, para o tratamento do tecido ósseo. Estes *scaffolds* foram produzidos através da técnica de impressão 3D *Robocasting*, com o intuito de estudar como esta tecnologia pode melhorar a produção de enxertos sintéticos, tornando-os mais compatíveis com cada paciente, explorando as suas limitações ao produzir diferentes geometrias.

Para a produção dos *scaffolds*, foi possível desenvolver pastas com uma reologia adequada para impressão 3D, alcançando 58wt% de sólidos. Através da formulação base, foram produzidas 4 geometrias diferentes, com propriedades mecânicas similares ao osso trabecular. Sendo a geometria Honeycomb que mais se destacou, por ser uma geometria complexa e por ter boas propriedades mecânicas. Com a incorporação de óxido de zinco e óxido de magnésio na formulação, as pastas de HAp-ZnO registaram uma diminuição de viscosidade. Através dos estudos realizados, os scaffolds HAp-ZnO obtiveram uma diminuição de porosidade e consequentemente um aumento das propriedades mecânicas superando resistência à compressão do osso trabecular. O grupo HAp-MgO registou um aumento de porosidade, que afetou diretamente as suas propriedades mecânicas. Contudo, quando submetidas a ensaios *in vitro*, as amostras de HAp-MgO apresentaram maior variação de peso e alterações na superfície em comparação com os restantes grupos.

Os resultados demonstram as capacidades de produzir *scaffolds* com diferentes geometrias e integrar diferentes biomateriais através da tecnologia *Robocasting*. Além disso, evidenciam como estas modificações impactam as propriedades microestruturais e mecânicas do *scaffolds*. Apontando um caminho promissor para a impressão 3D no desenvolvimento de enxertos personalizados para substituição óssea.

Palavras-Chave: Tecido ósseo; Impressão 3D; Forma dos poros; Hidroxiapatite; Óxido de Zinco; Óxido de Magnésio

Abstract

Bone problems and trauma affect millions of people worldwide and, with the increase in life expectancy, their prevalence is expected to continue rising. Metallic implants represent the gold standard in current treatments. However, in more severe cases, it becomes necessary to resort to bone substitutes, such as grafts. This approach faces several limitations, including limited availability, inadequate dimensions, and the risk of immune rejection. In this context, 3D printing emerges as an innovative solution, enabling the creation of synthetic grafts tailored to each patient, using biocompatible materials that promote bone regeneration, reduce complications, and accelerate recovery.

The aim of this study is to develop composite scaffolds based on hydroxyapatite, incorporating zinc oxide and magnesium oxide, for bone tissue treatment. These scaffolds were produced by Robocasting, with the objective to understand how this technology can improve the production of synthetic grafts, making them more compatible with individual patients and addressing their limitations by producing different geometries.

For scaffold production, it was possible to develop pastes with rheology properties suitable for 3D printing, achieving 58wt% solids. Using the base formulation, four different geometries were produced, with mechanical properties similar to trabecular bone. Among these, the Honeycomb geometry stood out for its structural complexity and excellent mechanical properties. With the incorporation of zinc oxide and magnesium oxide into the formulation, HAp-ZnO pastes showed a decrease in viscosity. Through the conducted studies, HAp-ZnO scaffolds exhibited reduced porosity and, consequently, improved mechanical properties, surpassing the compressive strength of trabecular bone. The HAp-MgO group exhibited an increase in porosity, which directly affected its mechanical properties. However, when subjected to *in vitro* tests, the HAp-MgO samples showed greater weight variation and surface alterations compared to the other groups.

The results demonstrate the ability to produce scaffolds with different geometries and integrate various biomaterials through Robocasting technology. Moreover, they highlight how these modifications impact the microstructural and mechanical properties of the scaffolds, indicating a promising pathway for 3D printing in the development of personalized scaffolds for bone treatment.

Keywords: Bone tissue; 3D Printing; Pore shape; Hydroxyapatite; Zinc Oxide; Magnesium Oxide

Table of Contents

Agradecimentos I
Resumo II
Abstract III
Table of Contents IV
List of Figures VI
List of Tables VIII
List of abbreviations IX
Chapter 1 - Introduction 1
1.1. Motivation 1
1.2. Problem identification 1
1.3. Goals 1
1.4. Organization of the Dissertation 2
Chapter 2 - Literature Review 3
2.1. Bone and fracture 3
2.2. Current treatment for bone tissue fractures 5
2.3. Scaffolds 6
2.4. Scaffolds Manufacturing 7
2.4.1. 3D printing/Additive manufacturing 8
2.4.2. Direct ink writing and Robocasting 9
2.5. Materials for Robocasting 10
2.5.1. Dispersant 10
2.5.2. Binder and plasticizers 11
2.5.3. Inorganic components 12
Chapter 3 - Materials and Methods 15
3.1. Materials 15
3.2. Production of ceramic pastes 15
3.2.1. Production of pastes with Magnesium oxide or Zinc oxide 16
3.3. Rheology characterization 16
3.4. 3D Modeling 17
3.5. Robocasting parameters and printing 18
3.6. Thermal Treatment 19
3.7. Scaffolds Characterization 20
3.7.1. Shrinkage, density and porosity 20

3.7.2. Compression Test 21
3.7.3. Scanning Electron Microscopy 21
3.7.4. Energy Dispersive Spectroscopy 22
3.7.5. Degradation test 22
Chapter 4 - 23
4.1. Powders Characterization 23
4.2. Paste Rheology 24
4.3. Scaffolds 27
4.3.1. Shrinkage, Density and Porosity 28
4.4. Morphological analyses 29
4.5. Compressive test 31
4.6. Result discussion 33
Chapter 5 - HAp-ZnO Scaffolds 35
5.1. Rheology 35
5.2. Scaffolds 36
5.2.1. Shrinkage, Density and Porosity 36
5.3. Microstructural analyses 37
5.4. Compressive test 39
5.5. Degradation test 40
5.6. Discussion of the incorporation of ZnO 42
Chapter 6 - HAp-MgO Scaffolds 45
6.1. Rheology 45
6.2. Scaffolds 46
6.2.1. Shrinkage, Density and Porosity 46
6.3. Microstructural analyses 47
6.4. Compression test 49
6.5. Degradation test 50
6.6. Discussion of the incorporation of MgO 52
Chapter 7 - Final discussion 55
Chapter 8 - Conclusion and future perspectives 59
8.1. Conclusion 59
8.2. Future perspectives 60
References 61

List of Figures

Figure 1 - Bone structure. A) femur, B) cortical and trabecular bone and C) extracellular matrix adapted from [1]. 3

Figure 2 - Bone trauma regeneration process, adapted from [1]. 4

Figure 3 - Additive manufacturing. A) SLA and B)FFF. Adapted from [20]. 9

Figure 4 - Direct ink printing. A) DIW and B) air, mechanical and screw types. Adapted from [23,24]. 9

Figure 5 - Process of Geometry Creation. A) cubic sample and B) Honeycomb Geometry. 17

Figure 6 - Geometries Obtained through PrusaSlicer. A) Diagonal, B) Orthogonal, C) Gyroid, and D) Honeycomb. 18

Figure 7 - Distribution of the Three Layers of the Honeycomb Geometry. A) 1st Layer, B) 2nd Layer, C) 3rd Layer, and D) Complete Scaffold. 18

Figure 8 - Thermal treatment cycle. 19

Figure 9 - SEM/EDS analysis of particles at 3000x magnification. A) HAp particles, B) ZnO particles, and C) MgO particles. 24

Figure 10 - Rheology paste with 40wt% HAp. A)influence of Darvan and B) values at 103 s^{-1}. 25

Figure 11 - Extrusion test with different concentrations of sorbitol. 26

Figure 12 - Rheology analysis with the increase of HAp solid percentage. 26

Figure 13 – HAp Scaffolds green bodies. A) Orthogonal, B) Diagonal, C) Gyroid and D) HoneyComb. 27

Figure 14 - Print error repair. A) before treatment and B) after treatment. 27

Figure 15 – HAp Scaffolds after thermal treatment. A) Orthogonal, B) Diagonal, C) Gyroid e D) HoneyComb. 28

Figure 16 – HAp Scaffold's Shrinkage. A) Volumetric lost and B) weight lost. 28

Figure 17 - HAp Scaffold's density after thermal treatment. 29

Figure 18 - HAp Scaffold's porosity of each geometry group. 29

Figure 19 - HAp Scaffold's SEM analysis 20x. A) Orthogonal, B) Diagonal, C) Gyroid e D) HoneyComb. 30

Figure 20 - HAp Scaffold's SEM Analysis. A)20x magnification, B) 100x magnification e C) 3000x magnification. 30

Figure 21 - HAp Scaffold's cross-section SEM low magnification analysis. A) Orthogonal, B) Diagonal, C) Gyroid e D) HoneyComb. 31

Figure 22 - HAp Scaffold's cross-section SEM high magnification analysis . A) 50x magnification and B) 3000x magnification. 31

Figure 23 - HAp Scaffold's Compressive test. A) Compressive curve, B) maximum compressive strength and C) Apparent compressive Stiffness. 32

Figure 24 - Rheology test of HAp-ZnO pastes. A) Viscosity-shear rate curve and B) Apparent printing viscosity. 35

Figure 25 - HAp-ZnO Scaffolds after thermal treatment. A) HAp and B) HAp-ZnO. 36

Figure 26 - HAp-ZnO Scaffold's shrinkage. A) Volumetric shrinkage and B) weight lost. 36

Figure 27 - HAp-ZnO Scaffold's density after thermal treatment. 37

Figure 28 - HAp-ZnO Scaffold's Porosity. 37

Figure 29 - HAp-ZnO Scaffold's SEM at 50x magnification. A) HAp , B) ZnO 1%, c) ZnO 2.5% and D) ZnO 5%. 38

Figure 30 - HAp-ZnO Scaffold's SEM/EDS at 5000x magnification. A) ZnO 1%, B) ZnO 2.5% and C) ZnO 5%. 39

Figure 31 - HAp-ZnO Scaffold's compressive Stress. A) Compression curve, B) Maximum stress and C) maximum compression stiffness. 40

Figure 32 - HAp-ZnO Scaffold's degradation test. 40

Figure 33 - HAp-ZnO Scaffold's SEM after degradation test. A) HAp, B) ZnO 1%, c) ZnO 2.5% and D) ZnO 5%. 41

Figure 34 - SEM/EDS of the HAp-ZnO. A) HAp (2000x), (B) ZnO 1% (2000x), C) ZnO 2.5% (2000x) and D) ZnO 5% (1000x). 42

Figure 35 - Rheology analysis of HAp-MgO pastes. A) Rheology curves and B) Apparent Printing viscosity. 45

Figure 36 - HAp-MgO Scaffolds after thermal treatment. A) HAp and B) HAp-MgO. 46

Figure 37 - HAp-MgO Scaffold's Shrinkage. A) Volumetric shringake and B) weight lost. 46

Figure 38 - HAp-MgO Scaffold's density after thermal treatment. 47

Figure 39 - HAp-MgO Scaffold's Porosity. 47

Figure 40 - HAp-MgO Scaffold's SEM at 100x magnification. A) HAp, B) MgO 1%, C) MgO 2.5% e D) MgO 5%. 48

Figure 41 - HAp-MgO Scaffold's SEM/EDS. A) MgO 1%, B) MgO 2.5% and C) MgO 5%. 49

Figure 42 - HAp-MgO Scaffold's compressive Test. A) Compression curve, B) maximum compressive strength and C) Compressive stiffness. 50

Figure 43 - HAp-MgO Scaffold's degradation test. 50

Figure 44 - HAp-MgO Scaffold's SEM analysis after degradation test (100x). A) HAp, B) MgO 1%, C) MgO 2.5% e D) MgO 5%. 51

Figure 45 - HAp-MgO Scaffold's SEM/EDS after degradation test (2000x). A) MgO 1%, B) MgO 2.5% and C) MgO 5%. 52

Figure 46 - Porosity of HAp and HAp composites. 55

Figure 47 - SEM/EDS of the HAp and HAp composites. A) HAp, B) HAp-ZnO 5% and C) HAp-MgO 5%. 56

Figure 48 - SEM/EDS of HAp and HAp composites after degradation test (2000x). A) HAp, B) HAp-ZnO 5% and C) HAp-MgO 5%. 57

List of Tables

Table 1 - Formulations of Ceramic Pastes for Robocasting 16
Table 2 - Printer Parameters for ByFlow Using PrusaSlicer. 19
Table 3 - Thermal treatment Parameters. 20
Table 4 - Viscosity of HAp and HAp composites pastes. 55
Table 5 - Scaffolds mechanical properties. 56

List of abbreviations

3D - Tridimensional

DIW - Direct ink writing

EDS - Energy Dispersive Spectroscopy

FFF - Fused Filament Fabrication

HAp - Hydroxyapatite

HAp-MgO - Hydroxyapatite/Magnesium Oxide composite

HAp-ZnO - Hydroxyapatite/ZnO Oxide composite

Mg - Magnesium

MgO - Magnesium Oxide

O - Oxygen

P - phosphorus

PBS - Phosphate Buffered Saline

pH – potential of hydrogen

PLA - Polylactic acid

PVA - Polyvinyl alcohol

SEM - Scanning Electron Microscopy

SLA - Stereolithography

wt% - Weight percentage

Zn - Zinc

ZnO - Zinc oxide

Chapter 1 - Introduction

1.1. Motivation

This work was developed with the aim of improving the treatment of complex bone fractures using Tridimensional (3D) printing technology. The use of this technology allows the production of patient-specific bone substitutes, designed with the patients' unique characteristics in mind. This study aims to apply the knowledge obtained from various studies and published articles on the use of biomaterials and 3D printing techniques for tissue regeneration, with a particular focus on bone tissue.

1.2. Problem identification

Bone performs several fundamental functions in our body and, in cases of trauma, has the ability to self-regenerate. However, for more complex fractures, surgical intervention becomes necessary. During the procedure, surgeons attempt to align and reconstruct the bone as precisely as possible. In most cases, metallic implants are used to connect the bone fragments. However, when the bone is fractured into more than two parts, these implants often prove insufficient, as small fragments are removed. To address this problem, bone grafts are used with the implants to fill the gaps, but in many instances, these grafts are inadequate or even cause rejection by the body. Therefore, this dissertation aims to address this issue by using 3D printing and biocompatible materials to improve treatment outcomes.

1.3. Goals

With this work, the objective is to produce Hydroxyapatite (HAp) scaffolds using the 3D Robocasting printing technique, testing the capabilities of 3D printing for the customization and production of synthetic bone grafts. In addition, it aims to enhance their mechanical and regenerative properties through the creation of various geometries and produce scaffolds composites with the addition of Zinc Oxide (ZnO) and Magnesium Oxide (MgO).

1.4. Organization of the Dissertation

The dissertation is divided into six main chapters and their respective subsections, in order to facilitate reading and make the content more accessible. This first chapter aims to introduce the topic, objectives, and structure of the work, providing a foundational understanding of the elements that will be explored throughout the dissertation.

Chapter 2 presents a literature review on the subject, beginning with an overview of the skeletal system anatomy, an analysis of fractures, and bone regeneration. It then proceeds to review current fracture treatment methods and, consequently, the exploration and application of 3D printing in this field. This chapter also details the various compounds incorporated into the pastes used for 3D printing of scaffolds.

Chapter 3 is organized into several sections, presenting the materials and methodology used in this study. The materials employed are listed in detail, followed by a description of the process for preparing the ceramic pastes for Robocasting. In the section on 3D printing, the various geometries and parameters implemented in the printer are presented. Additionally, this chapter outlines the characterization techniques applied throughout the study.

The following chapters present the results obtained in this dissertation. Chapter 4 focuses on scaffold production and the effect of geometry. It begins with particle analysis and a series of rheology studies, leading to the establishment of the base formulation. This is followed by scaffold characterization before and after thermal treatment, compression testing, and SEM analysis. The chapter concludes with a discussion consolidating all results obtained. Chapter 5 is dedicated to the production of scaffolds composites incorporating ZnO (HAp-ZnO), while Chapter 6 addresses the scaffolds incorporated with MgO (HAp-MgO). These two chapters follow a structure like Chapter 4, with the addition of degradation test results and their corresponding SEM/EDS analyses. Each of the 3 chapters also includes a concluding discussion. To allow for a comprehensive comparison and discussion of results from all three chapters and their alignment with existing literature, Chapter 7 was created.

Finally, the last chapter consists of the conclusion and future perspectives. It offers a final reflection on the entire body of work, consolidating the results and discussions presented in the previous chapters. This section explores the challenges encountered throughout the dissertation and in the 3D printing process, and consequently proposes potential ideas for future research investigations.

Chapter 2 - Literature Review

2.1. Bone and fracture

The human skeleton is the internal framework of the body responsible for supporting the body, protecting vital organs, and providing a system for movement. In addition, bones play an important role in the body's systems containing bone marrow, which produces blood cells, and also in the body's regulation of the levels of calcium (Ca) [1].

On a macro level, bone (Figure 1) can be divided into two components: cortical bone and trabecular bone(Figure 1.B). In structural terms, cortical bone is located more at the extremities of the bone and its denser, with a porosity ranging from 5% to 30%, whereas trabecular bone is located at the interior of the bone, with a fully porous interconnected structure with a porosity that starts at 30% but in some reach can reach up to 90%. As a result, cortical bone primarily supports a significant portion of the load applied to human skeleton, thereby providing protection to the internal tissues. Cortical bone displays a compressive strength ranging from 130 to 225 MPa, while trabecular bone displays a strength of approximately 7 to 10 MPa [1], [2].

In terms of physiology, trabecular bone plays an important role in the production and storage of bone marrow, which is essential to produce blood cells. In contrast, cortical bone serves another significant function beyond protection: it acts as a reservoir for minerals such as Ca and phosphate, which are vital for various functions within the human body [1].

Furthermore, the skeletal system is defined by the composition of the extracellular matrix (Figure 1.C). Bone is composed of an organic component (primarily collagen and proteoglycans) accounting for approximately 30%, while the remaining portion consists of an inorganic component made up of minerals such as calcium phosphates, predominantly in the form of hydroxyapatite. The collagen fibers serve to provide flexibility to the bone, while the mineral component imparts mechanical strength to the bone [1], [3].

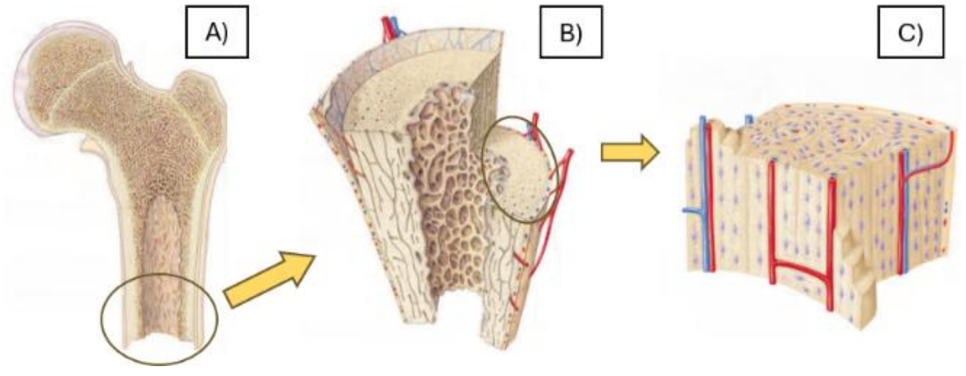

Figure 1 - Bone structure. A) femur, B) cortical and trabecular bone and C) extracellular matrix adapted from [1].

At the cellular level, osteoblasts are responsible for creating, repairing, and remodeling bone tissue. During the process of bone formation (also known as ossification), osteoblasts become embedded in the bone extracellular matrix, maturing into cells known as osteocytes. The bone matrix and the osteocytes are represented in Figure 1.C. To maintain homeostasis, both in the skeletal system and throughout the body, constant bone remodeling is required. This is where osteoclasts come into play, as they are responsible for bone destruction and absorption. Due to the bone's ability to store minerals, this resorption process helps stabilize mineral levels in the body in cases of deficiency [4], [5].

In the event of trauma or an accident, a bone fracture may occur. These fractures are classified as either open or closed, depending on whether there is a breach of the skin. However, additional factors such as the location, complexity, morphology, and severity of the fracture further influence the diagnosis. Consequently, fractures can be categorized as complete, incomplete, or comminuted [1].

In the case of fracture, similarly to the bone homeostasis process, bone initiates a process of regeneration (Figure 2). In addition to the fracture, the surrounding blood vessels are also damaged. The process begins with bleeding, which triggers an inflammatory response, leading to the formation of a hematoma in the affected region (Figure 2.A). Within a few days, cells and blood vessels start to infiltrate the damaged region, and the cells begin forming interconnected fibers and cartilage to bridge the damaged bone parts. This stage is referred to as the formation of a callus (Figure 2.B). Between 4 and 6 weeks after the fracture, osteoblasts generate trabecular bone in the affected area (Figure 2.C). Finally, over time, this bone gradually transforms into cortical bone until the fracture is fully healed (Figure 2.D). This process can take several months, depending on the severity of the case [1], [6].

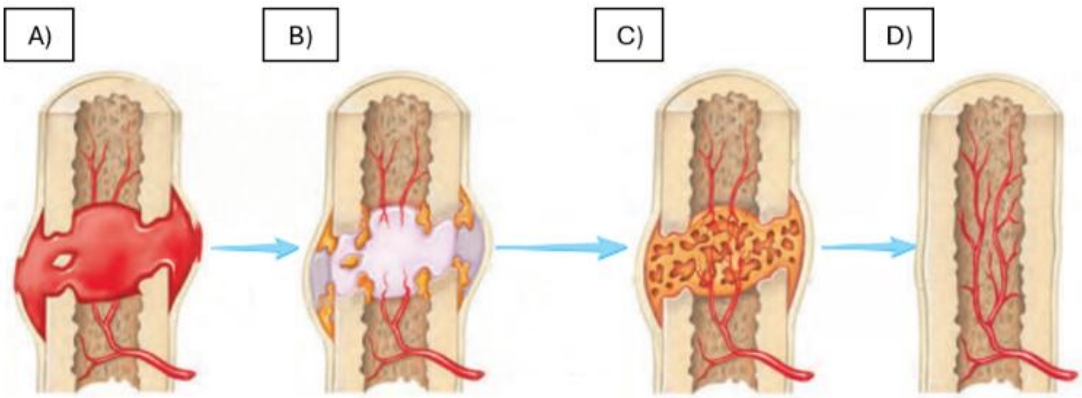

Figure 2 - Bone trauma regeneration process, adapted from [1].

2.2. Current treatment for bone tissue fractures

Despite bone's excellent regenerative capabilities, in more complex cases such as open, complete, or comminuted fractures, surgical intervention is necessary to assist in the reconstruction and recovery process. During medical intervention, surgeons attempt to align and reconstruct the bone as much as possible and use metal implants to connect the fragments. However, in the case of comminuted fractures, where bone is broken into more than two parts and/or multiple small fragments are present, these implants are often insufficient, as the small fragments are usually removed due to the difficulty of securing implants to them [1], [7].

One of the most common alternatives is the use of grafts. However, despite several years of use, these methods still present various disadvantages. The gold standard is the autograft technique, which involves harvesting grafts from the patient's own body. The inherent drawbacks of this approach are evident, because harvesting tissue from the patient necessitates careful attention to avoid worsening the existing condition, resulting in a limited supply of graft material. Consequently, multiple surgeries are often required due to the small quantity that can be harvested in a single procedure [7], [8].

Other techniques include allografts, which involve grafts harvested from another individual, whether from a cadaver or a donor. And xenografts, which use parts of another species to create bone grafts. While these techniques may provide more readily available resources, it carries the disadvantage of potential rejection by the body or the risk of pathogen transmission [8].

Factors such as advancing age and diseases that affect the capacity for bone remodeling, such as osteoporosis and cancer, diminish the bone's ability to self-regenerate and weaken the immune system. This leaves individuals increasingly susceptible to fractures in the event of an accident, a situation that is becoming more common as life expectancy increases. Consequently, the risk of infections and rejection of implants and grafts becomes even greater, leading to more post-surgery complications [7], [9].

As a result, one of the alternatives that bone tissue engineering has been exploring over the past decades is the implantation of inorganic or synthetic grafts, commonly referred to in the literature as scaffolds, to place in the areas of the bone that are incomplete, rather than relying on traditional graft types.

2.3. Scaffolds

According to the literature about bone tissue engineering, a scaffold can be defined as a matrix that provides structure and an appropriate environment for bone growth. In this context, scaffolds are synthetic grafts designed to mimic bone tissue and stimulate the growth of new bone cells, acting as osteoconductive materials. Their primary aim is to reconstruct the missing region by promoting bone regeneration [8].

With this in mind, the development of scaffolds must follow specific criteria to ensure the effectiveness of bone fracture treatment. a) Scaffolds must be biocompatible, ensuring low toxicity and minimizing inflammatory responses throughout the healing process. b) Scaffolds should have strong mechanical properties, and, if necessary, be biodegradable. c) During the initial weeks, it must maintain structural integrity to support the various forces acting on the fracture region, while also degrading in a controlled manner to create space for the formation of new bone tissue and d) The scaffold should have a suitable porous architecture, allowing it to adapt well to the fracture site and enabling the movement and expansion of cells and nutrients [10].

Scaffold's porosity is one of the most critical characteristics to consider in their development. As highlighted in reviews by Marques et al. and Abbasi et al. about the subject, creating scaffolds with adequate and fully interconnected porosity enhances cell adhesion and facilitates the transport of cells and nutrients throughout the affected region, thus accelerating the bone reconstruction process. Suggested values indicate that pore sizes between 300 and 500 μm provide better connections with osteoblasts, thereby improving osteogenesis. Furthermore, pores smaller than 100 μm promote the formation of the non-mineralized components of bone and fibrous tissue. In other words, developing scaffolds with varying levels of porosity helps to reconstruct different bone components, allowing them to be interconnected to achieve optimal mechanical and biological properties [11], [12].

Even if the scaffold is manufactured with the appropriate dimensions, if its surface and interior do not provide a favorable environment for cell adhesion and development, it could hinder rather than support the regeneration process. Therefore, it is essential to carefully consider the used biomaterials to ensure that the scaffold effectively improves cellular activity and promotes bone healing.

Inorganic materials are among the most extensively studied, due to their similarity to bone's mineral component, particularly calcium phosphates. However, as ceramic materials, they lack significant plastic behavior compared to other materials such as metals and polymers, which makes them quite brittle. As a result, they tend to fracture with minimal prior deformation when subjected to high loads [3]. Natural-origin biomaterials exhibit characteristics similar to bone tissue, enhancing cell adhesion and migration on both the surface and within the scaffold. Mechanically, while they tend to offer greater flexibility compared to inorganic materials, they generally have even less capacity to withstand high stresses, making them less suitable for load bearing applications [13].

Synthetic materials offer several relevant characteristics for the development of bone substitutes, including good stiffness, elasticity, and microscale composition. However, when used alone, they typically exhibit low bioactivity, which can hinder tissue regeneration. Furthermore, their degradation can, in many cases, release toxins into the body, posing additional risks to the healing process [3], [14].

Therefore, in the development of bone substitutes, it is important to combine different types of biomaterials, this combination can enhance the properties where each biomaterial type lacks. Resulting in a scaffold with optimal mechanical and biological characteristics [13], [14].

2.4. Scaffolds Manufacturing

For scaffold manufacturing, there are various techniques available, which can be broadly divided into conventional methods and additive manufacturing.

Among the conventional techniques, some of the most explored include gas foaming and polymer sponge replication [2], [15]. Gas foaming is a technique that creates porous structures through the formation of air passages and bubbles within the material. Initially, the desired mixture is prepared by adding foaming agents. After the scaffold is molded and submerged in a solution that triggers a chemical reaction with the foaming agents, resulting in the formation of porosity within the structure [2]. In the sponge replication technique, first the ceramic paste is impregnated into a sponge mold. After drying, this mold undergoes a thermal treatment, during which the sponge is removed and the scaffold is sintered, resulting in a completely porous final sample. It is crucial to ensure that the sponge is thoroughly impregnated to prevent any voids within the structure, as these can diminish its overall properties [15].

Currently, biodegradable synthetic scaffolds are produced and marketed as surgical options derived from these conventional techniques [16]. However, these methods have significant limitations, as it is challenging to control the scaffold's porosity and pore geometry, resulting in standardized, industrialized models with no customization for individual patients. Since these techniques rely on specific molds and forms for manufacturing, creating a unique mold for each case would be prohibitively expensive and time-consuming [17].

So, to produce scaffolds that are customizable for each patient, increasing stability, biocompatibility and outcome the disadvantages of the current manufacturing techniques. This is where additive manufacturing comes into play, offering the potential to produce customized scaffolds through 3D printing.

2.4.1. 3D printing/Additive manufacturing

Additive manufacturing, commonly known as 3D printing, emerged in the late 1980s, with the patent for the Stereolithography (SLA) method registered in 1984 by Charles Hull [18]. Through this method, Hull utilized a liquid photopolymer and UV light to produce thin layers of solid material (Figure 3.A). This innovation laid the foundation for 3D printing, where objects are first digitally designed, followed by the development of printing code, and ultimately produced layer by layer in the printer until the final shape is achieved. As a result, this technique has gained recognition as a process capable of creating objects with a low material waste rate and complex geometries that surpass those achievable through conventional manufacturing [18], [19].

Based on this premise, interest in this technique has grown over the years, leading to the development of multiple 3D printing methods. This expansion has moved from the initial use of liquid photopolymers to a nearly infinite range of materials [19]. One of the areas that extensively explores the use of this technique is biomedical engineering. With this method, the possibility of developing customizable solutions for patients arises, eliminating the need for pre-made molds for production [20].

The most widely explored and utilized technique is Fused Filament Fabrication (FFF) (Figure 3.B), which employs a heated nozzle to deposit a heat-softened polymer (such as Polylactic Acid(PLA)) directly onto a base, layer by layer [19]. In the field of bone regeneration, this method has been explored for the creation of bone substitutes, as PLA is a biocompatible material. However, it has the disadvantage of a low degradation rate. Consequently, research is being conducted on modifications to the PLA filament itself or the addition of a coating after printing to accelerate the degradation process [21].

Since FFF focuses on the use of solid materials that melt at a certain temperature and return to a solid state at room temperature, there arose a need to develop alternatives for materials that are not susceptible to such temperatures, or for the incorporation of biological materials that would be destroyed or severely altered in this type of printing. As a result, Direct ink writing (DIW) was developed [19], [22].

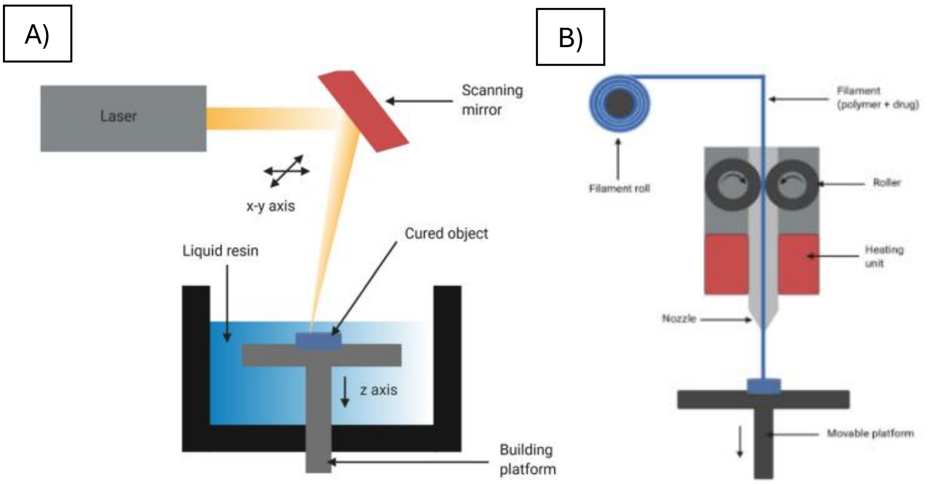

Figure 3 - Additive manufacturing. A) SLA and B)FFF. Adapted from [20].

2.4.2. Direct ink writing and Robocasting

DIW is considered an evolution of the FFF technique, enabling increased research across various fields of bioengineering [22]. This technique utilizes concentrated suspensions, also known as pastes. These pastes are extruded in filament form through a nozzle under pressure (Figure 4.A) [23], [24]. Direct Ink Printing methods can be classified by their extrusion mechanisms, which are categorized into air, mechanical, and screw types (Figure 4.B) [22]. In the air mechanism, the extrusion process is entirely controlled by pressurized air that extrudes the paste in a regulated manner. In the case of the mechanical type, a linear-moving piston controls the volume of paste extruded. Lastly, the screw type relies on the rotation of a screw to influence the extrusion of the paste [23].

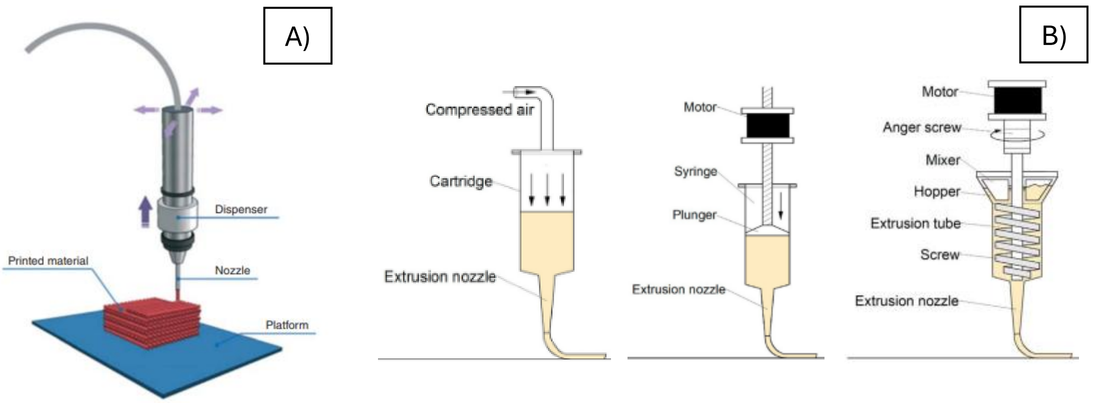

Figure 4 - Direct ink printing. A) DIW and B) air, mechanical and screw types. Adapted from [23,24].

A variant of DIW is Robocasting, which aims to print ceramic pastes or dense ceramic composites. In this process, Robocasting primarily relies on the rheology of the material and its ability to flow during extrusion under high stress while partially drying shortly after extrusion when the stress decreases. This allows Robocasting to support the printing of denser objects with superior mechanical properties, offering advantages for the printing of scaffolds intended for bone regeneration [25], [26], [27].

2.5. Materials for Robocasting

As previously mentioned, 3D printing of scaffolds has been explored in recent years due to its ability to produce bone substitutes with complex geometries capable of simulating damaged bone areas and creating intricate 3D networks that mimic the spongy region of bone.

For robocasting, it is essential to ensure stability during the printing process, thereby guaranteeing printability with minimal defects. This involves producing a pseudoplastic paste (a non-Newtonian fluid) that exhibits high viscosity when at rest and reduced viscosity when subjected to pressure or agitation [23]. In order to extrude smoothly and ensure that the paste maintains its shape upon deposition, it must be capable of supporting all the layers that will be printed [27]. Consequently, materials play a fundamental role, given that the paste contains a high solid content, it is necessary to incorporate specific components to facilitate and ensure stability. Typically, additives such as dispersants, binders, and plasticizers are included in the formulations for this purpose [26].

2.5.1. Dispersant

The dispersant is an additive whose purpose is to separate agglomerated particles in a solution, ensuring uniform particle distribution throughout the mixture, thereby reducing viscosity and stabilizing the formulation. This also allows for an increased solid content in the paste while ensuring its printability.

Darvan

Darvan, also known as sodium polyacrylate, is a dispersant agent utilized in the production of ceramic formulations. Its purpose is to improve viscosity and enhance stability, ensuring that ceramic particles are well distributed and do not agglomerate [28].

In the case of robocasting, Darvan 811 and its variants are among the most used in studies, especially when HAp is the selected ceramic. The use of dispersants in robocasting not only serves the previously mentioned purposes but also aids in increasing the solid content within the formulation. When producing scaffolds, it is essential to achieve the highest possible solid content to enhance the mechanical properties [29].

2.5.2. Binder and plasticizers

In the case of binders and plasticizers, these additives, although acting differently within the paste, serve a similar purpose by focusing on the stability of the paste. The binder's function is to bond the various materials in the paste, while the plasticizer's role is to control the paste's texture, improving its flow and maintaining its shape once extruded. Together, these two additives simplify the extrusion process by helping ensure that the filaments do not break during extrusion and drying, preserving the printed form [26].

Another factor regarding these additives is that, depending on the paste produced and the materials used, the same additive can function as a binder in one case and as a plasticizer in another. According to Monfared et al., certain materials, such as Carboxymethyl cellulose and Pluronic F-122, have the capability to perform both functions. Another material that performs both functions but stands out as a binder is Polyvinyl Alcohol (PVA) [26].

Polyvinyl Alcohol

PVA is known for being a versatile synthetic polymer with excellent mechanical and biological properties. According to Monfared et al., the advantages of PVA include good biocompatibility, water solubility, and low toxicity. In the production of PVA, the degree of hydrolysis is a crucial factor, which can be partially (80-98.5%), highly (> 98.5%), or fully (100%) hydrolyzed. The type of production alters the macromolecular chains of PVA, directly impacting its mechanical and chemical properties [30]. One factor that is affected by hydrolysis is its water solubility, which is higher at lower temperatures with a lower degree of hydrolysis and increases at higher temperatures (above 70ºC) when the PVA is highly hydrolyzed [31]. One of its issues is its biodegradability, which can differ significantly depending primarily on the environment in which it is placed, the materials it is combined with, and its low cell-adhesive properties [31].

In terms of robocasting, PVA is used as a binder due to its ability to stabilize ceramic solutions with a high solid content through electrostatic forces, as it is a polyelectrolyte material. This enhances the cohesion within the paste, aiding in the drying process of the piece and reducing the likelihood of cracking [26].

Sorbitol

Sorbitol, also known as glucitol, is a biomaterial naturally found in plants and fruits. It is widely used in the fields of food, cosmetics, and even biomedicine. In terms of production, sorbitol is primarily obtained through the catalytic hydrogenation of glucose, using starch or cellulose as the base material [32], [33].

As a sugar alcohol, sorbitol possesses excellent properties, being highly stable and soluble in water, with good biocompatibility and degradability. Sorbitol can be utilized in 3D printing or robocasting due to its function as a plasticizer, helping to reduce the viscosity of the paste and making it more fluid [34]. Sorbitol appears to be a highly promising material for robocasting; however, there are currently few studies on the addition of sorbitol with ceramics as a plasticizer. Its use is commonly observed in the 3D printing of edible products, as demonstrated in the work of Falcone et al., who produced tablets through 3D printing using sorbitol as a plasticizing agent in the formulation [35].

2.5.3. Inorganic components

The inorganic component serves a crucial role in robocasting, particularly when the printing of scaffolds involves thermal treatment to enhance their properties, as it is the only material remaining after this process. The use of ceramics and bioglass as base materials, along with certain metals and oxides to improve mechanical and biological properties, is extensively studied for bone regeneration [3].

Hydroxyapatite

Hydroxyapatite (HAp), chemicaly known as $Ca_{10}(PO_4)_6(OH)_2$, is a bioceramic that has been extensively studied due to its chemical and physical characteristics, which are similar to the inorganic phase of bone. As mentioned earlier, it is composed of calcium phosphate crystals. Synthetic HAp does not have the same ion composition and crystal orientation compared to biological HAp. However, it remains a highly stable biocompatible material that is osteoconductive and promotes the formation of new bone tissue [36].

In addition to bone grafts, HAp has been explored in tissue regeneration applications, including implant coatings and even as a drug delivery system [37]. As an implant coating, HAp has proven highly effective and has been widely studied, with early successful applications like that of Darimont et al. (2002), who implanted an HAp-coated titanium implant into a rabbit, reporting enhanced contact and stability between the bone and implant [38]. This illustrates the long-standing interest in HAp's role in bone tissue engineering.

However, there are certain limitations in the use of HAp, especially for bone grafts. Due to its high stability within the human body, HAp exhibits a notably low degradation rate, which may impede early stages of bone regeneration within the first few weeks [37], [39]. Additionally, Lelo et al. refer that HAp's mechanical properties are lower than the cortical bone ones, and are closer to the trabecular bone, which makes it a less suitable option for standalone use as bone grafts substitute, particularly in body regions subjected to higher mechanical forces [39].

Magnesium Oxide

Magnesium Oxide (MgO) is a biomaterial studied in tissue engineering, particularly in the production of orthopedic implants and prostheses. The interest in magnesium (Mg) arises from its status as one of the most abundant minerals in the human body, particularly in bone [40], [41]. MgO possesses excellent properties, being biocompatible, biodegradable, readily available, and cost-effective [42]. MgO contributes to the adhesion of osteoblasts on the surface of the material through the release of Mg^{2+} ions, accelerating bone regeneration in the affected area. Furthermore, two studies by Coelho et al. report that MgO, in conjunction with HAp, exhibits antibacterial and angiogenic properties. And Chen et al. describe that Mg ions have the capacity to accelerate the degradation of the material, which is particularly beneficial for substances like HAp that exhibit a low degradation rate.

In mechanical terms, it is reported that MgO can enhance factors such as maximum load stress and Young's modulus of scaffolds. However, Chen et al. note that, despite the general acceptance of this improvement in properties, this effect may be more closely related to the distribution of particles in the formulations. Factors such as particle shape and structure could be the true determinants of this enhancement [43].

Zinc Oxide

Zinc Oxide (ZnO) is known for its versatility, being studied in various fields ranging from electronics to numerous biomedical applications. It possesses piezoelectric and conductive properties, making it of interest to produce semiconductors and biosensors [44]. It is biocompatible and antibacterial, making it suitable for wound treatment. Additionally, it possesses excellent mechanical properties, enhancing the strength of biomaterials designed to withstand forces [45], [46]. In the development of scaffolds, specific benefits from using ZnO have also been recorded. According to the study by Feng et al., the incorporation of ZnO in calcium phosphate scaffolds resulted in increased compressive strength and stiffness. Biologically, there was also an enhancement in cell adhesion and proliferation on the surface of the scaffold compared to the control sample [47].

In their review, Chen et al. emphasize on zinc (Zn) in bone regeneration that the use of Zn and ZnO in the development of scaffolds enhances degradation properties, increases osteogenesis, and highlights antibacterial properties along with a reduction in post-operative infections [43].

Although Zn is recognized as the second most abundant element in the human body, it is important to note that the release of Zn ions in excessive concentrations induces cytotoxicity, regardless of whether it is ZnO or another material containing Zn. Therefore, it is crucial to exercise caution regarding the amount of ZnO incorporated into scaffolds and to study the thresholds to ensure that the scaffold continues to support bone regeneration rather than hindering it [43], [44].

Chapter 3 - Materials and Methods

Based on the premise explored in the literature review, this section advances to the experimental work developed in this study: the production of HAp scaffolds using the Robocasting technique. This chapter details all the steps involved, starting with the preparation of the pastes and the additives used, as well as the incorporation and preparation of HAp-ZnO and HAp-MgO pastes. Additionally, the steps required to obtain the final 3D-printed green body, and its corresponding thermal treatment. Finally, all the tests performed to analyze the geometries employed and the incorporated materials are presented.

3.1. Materials

Hydroxyapatite (purum p.a. ≥90%) was purchased from sigma-Aldrich (Missouri, EUA). Darvan811 (sodium polyacrylate solution, 40 – 45%vol) was purchased from Vanderbilt Chemicals (Connecticut, EUA). Magnesium oxide (ACS reagent 97%) was purchased from sigma-Aldrich (Missouri, EUA). Zinc oxide (ACS reagent ≥99%) was purchased from sigma-Aldrich (Missouri, EUA). D-Sorbitol (≥98% pure) was purchased from sigma-Aldrich (Missouri, EUA). PVA (87-89% hydrolyzed) from sigma-Aldrich (Missouri, EUA). PBS (10x solution) was purchased from Fisher Bioreagents (Geel, Belgium).

3.2. Production of ceramic pastes

To produce various ceramic pastes, a formulation of HAp was developed. It is important to note that the PVA used for this purpose was not added directly, but rather derived from a 20wt% PVA solution, prepared over 48 hours at 80°C. After the first 24 hours, a manual mixing process was employed to homogenize the solution, and this process was repeated three times. Once homogeneous, the solution is ready for use.

Initially, Darvan was added to the necessary amount of distilled water and subsequently stirred. Following this, HAp was gradually added, and when mixing became difficult, sorbitol was introduced to reduce the viscosity. Once this step was completed, the PVA solution was added. After the paste was produced, it was set aside to ensure the elimination of air bubbles. The material percentages of the base formulation are listed in Table 1.

3.2.1. Production of pastes with Magnesium oxide or Zinc oxide

To enhance both the physical and biological properties of the scaffolds, ZnO and MgO were added. In producing these pastes, adjustments were made to the amount of HAp while consistently maintaining the same quantity of the inorganic material at 58wt%. For each material, three distinct pastes were produced with concentrations of 1wt%, 2.5wt%, and 5wt%. Regarding the production of these pastes, the difference lies in the initial addition of MgO or ZnO to the Darvan solution (prior to the addition of HAp), followed by stirring for 10 minutes. The different pastes produced in this study are represented in Table 1.

Table 1 - Formulations of Ceramic Pastes for Robocasting

Formulation (wt%)	HAp	ZnO	MgO	Sorbitol	Darvan	PVA
HAp (control)	58	-	-	5	2	1.5
ZnO 1%	57	1	-	5	2	1.5
ZnO 2.5%	55.5	2.5	-	5	2	1.5
ZnO 5%	53	5	-	5	2	1.5
MgO 1%	57	-	1	5	2	1.5
MgO 2.5%	55.5	-	2.5	5	2	1.5
MgO 5%	53	-	5	5	2	1.5

3.3. Rheology characterization

To study the correct percentages of the paste and its limitations, rheology tests were conducted. The viscosity of the pastes was measured using the rheometer from Anton Paar, model MCR 92, conducting a viscosity-shear rate study. Initially, the maximum solid limit was achieved using only HAp and distilled water. With the maximum value reached, the correct percentage of dispersant in the paste was then studied, selecting the paste with the lowest viscosity. Following this selection, a new test was conducted to determine the upper limit for the addition of HAp.

After determining the new maximum solid content, the final paste was produced by adding sorbitol and PVA, followed by rheology testing of the mixture. With the addition of these materials, printability tests were conducted, during which filaments were produced using a syringe and allowed to dry. This is because not only low viscosity is important, but also the stability of the paste after drying. Finally, with the control formulation achieved and good print quality ensured, pastes containing ZnO and MgO were produced, and their rheology tests were conducted. In order to understand the shear rate to which the paste is subjected during printing, its apparent shear rate can be obtained through eq.(1).

$$Apparent\ shear\ rate\ (\gamma^{\cdot}) = \frac{4*Qmax}{\pi*R^3} \tag{1}$$

Where $Qmax$ is the maximum volumetric speed of the printing and R the radius of the extruder nozzle. These values used are acquired after optimization of the printed parameters.

3.4. 3D Modeling

As mentioned in the literature review, geometry plays an important role in the development of scaffolds. Given this, geometry opens possibilities for comparisons at various stages of the work, from its behavior during robocasting printing, studying the printer's limits, to its behavior during thermal treatment and the examination of its mechanical properties, thereby understanding how geometries influence the mechanical resistance of the scaffolds.

For this process, the *PrusaSlicer* software was used, which, through a cubic sample measuring 12x12x8 mm and in conjunction with the infill tool, allows for the creation of various geometries. In Figure 5, shows how the cubic sample (Figure 5.A) transited to the desired geometry in the program (Figure 5.B). However, not all geometries used in this study had perfect direct transition, and it was necessary to modify several parameters, like the fill angle, to guarantee the stability of the scaffold during and after printing.

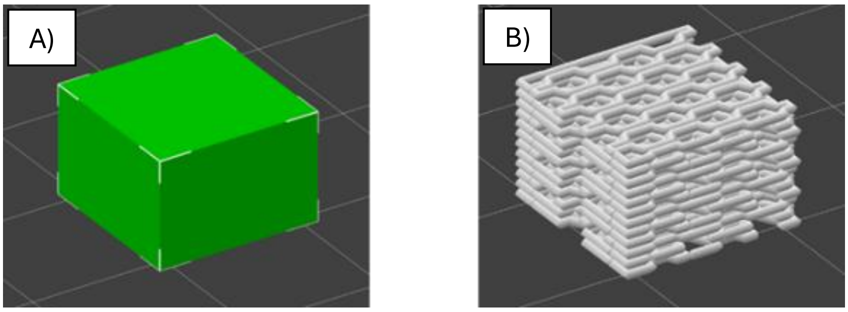

Figure 5 - Process of Geometry Creation. A) cubic sample and B) Honeycomb Geometry.

Taking this into consideration, four geometries were selected for study (Figure 6). The Orthogonal and Diagonal geometries present a simpler structure, consisting of straight filaments, with the only difference being the printing angle. In contrast, the Gyroid and Honeycomb geometries are more complex structures, where the filaments take on curved shapes and angle variations within a single layer.

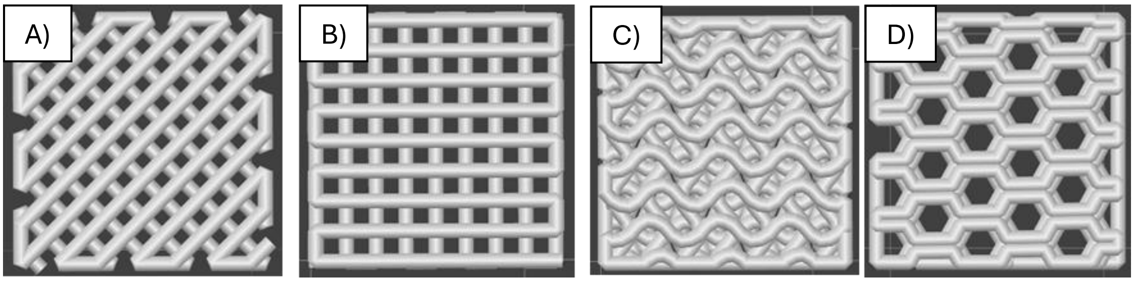

Figure 6 - Geometries Obtained through *PrusaSlicer.* A) Diagonal, B) Orthogonal, C) Gyroid, and D) Honeycomb.

Another difference lies in the layering of the Gyroid and Honeycomb. In the two simpler geometries, each layer is rotated 90º from the previous one. In contrast, the Honeycomb geometry consists of three distinct layers that repeat in order, as shown in Figure 7. In the case of the Gyroid, there is no set order, as all layers differ from one another.

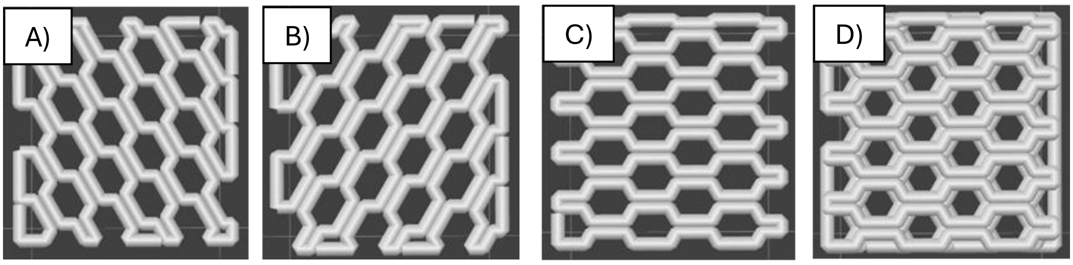

Figure 7 - Distribution of the Three Layers of the Honeycomb Geometry. A) 1st Layer, B) 2nd Layer, C) 3rd Layer, and D) Complete Scaffold.

3.5. Robocasting parameters and printing

After optimizing the pastes and developing the CAD models, the process moved on to 3D printing. For this purpose, the printer from ByFlow (Eindhoven, Netherlands) was used. This printer has the ability to use both FFF and robocasting tools, enabling the printability of different materials.

The optimization of the printer parameters was also performed with the help of *PrusaSlicer* software, creating a profile that recorded all the machine's properties, including size, printing limits, speed, extruder size, and more. This approach made it possible to create files tailored to the printer and test its limits. The optimized parameters are described in Table 2.

Table 2 - Printer Parameters for ByFlow Using *PrusaSlicer*.

Building size (mm)	200 x 200 x 180
Printing speed (mm/s)	1 - 5
Nozzle size (mm)	0.6
Layer height (mm)	0.65
Extrusion width (mm)	0.65
Infill density (%)	50
Vertical/horizontal shells	none

After the optimization phase, 15 samples for each of the different geometries were produced. They were placed in a humid environment for the first 24 hours, allowing for a slower drying process and reducing the chances of cracking. The samples were then subjected to thermal treatment and mechanical testing to evaluate which structure performed best mechanically. It is important to note that the results from the different geometries will be used to select the most suitable one for printing with the various concentrations of ZnO and MgO mentioned in section 3.2.1. For that part of the work, 20 samples for each formulation listed in table 1 were produced.

3.6. Thermal Treatment

With the printing of the samples and their drying in a humid environment completed, the next step is the preparation for their thermal treatment. In this stage, the samples are first placed in the oven (Binder ED23) at 60°C for one day. Subsequently, measurements and weighing of each green body are conducted before placing them in the oven from TERMOLAB. Two stages were programmed: the first stage is debinding, which burns off all temperature-sensitive materials, including Darvan, sorbitol, and PVA. The second stage is the sintering of HAp. The temperatures and duration for each stage are described in Table 3 and in Figure 8.

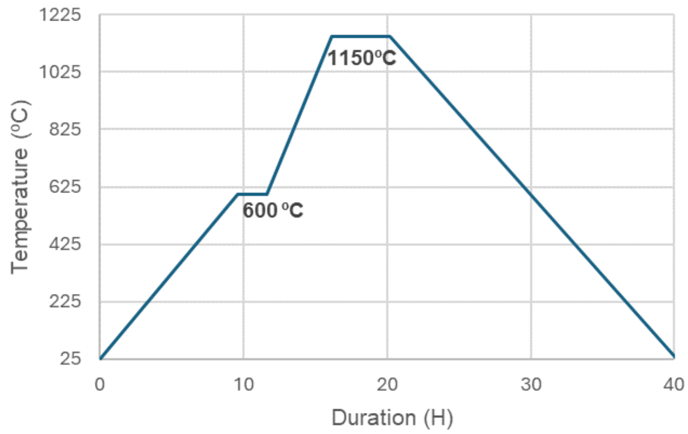

Figure 8 - Thermal treatment cycle.

Table 3 - Thermal treatment Parameters.

Thermal Cycle	Temperature	Dwell
Debinding	1ºC/min -> 600ºC	2 hours
Sintering	2ºC/min -> 1150ºC	4 hours

3.7. Scaffolds Characterization

3.7.1. Shrinkage, density and porosity

With the completion of the thermal treatment, the next step before scaffolds mechanical characterization, was to measure each sample to study its behavior during the thermal treatment. First, all sides were measured, and the samples were weighed before and after the thermal treatment. With these values, it was possible to determine the shrinkage (eq. 2) and weight loss (eq. 3)

$$Shrinkage\ (\%) = \frac{Vi - Vt}{Vi} \times 100 \quad (2)$$

$$Weight\ lost\ (\%) = \frac{Wi - Wt}{Wi} \times 100 \quad (3)$$

Where in eq. (2) Vi is the green body volume and Vt the scaffold volume after debinding and sintering. For eq. (3) Wi is green body weight and Wt the scaffold weight after treatment. Moreover, the apparent density was determined by eq. (4) and the bulk density of the samples was calculated using Archimedes' principle and an analytic balance (A&D GR-200-EC) with a determination density kit (A&D AD-1653). By weighing the object in air and submerged in water, its bulk density was determined using eq. (5).

$$Apparent\ density\ (g/cm^3) = \frac{Weight}{ApVolume} \quad (4)$$

$$Bulk\ density\ (g/cm^3) = \frac{Wair}{Wair - Wwater} \times \rho water \quad (5)$$

Where in eq. (4) $Weight$ and $ApVolume$ is the scaffold weight and apparent volume after thermal treatment. $Wair$ in eq. (5) is the scaffold after treatment weight, $Wwater$ the scaffold weight in water and $\rho water$ is the water density at the exact temperature during the test. Finally, to determine the porosity of the samples after thermal treatment, eq. (6), (7) and (8) were used. These formulas allow for the calculation of the total porosity and the bulk porosity of each sample based on the apparent density and the bulk density calculated previously with the theoretical value.

$$Total\ porosity\ (\%) = \left(1 - \frac{\rho apparent}{\rho teoric}\right) \times 100 \tag{6}$$

$$Bulk\ porosity\ (\%) = \left(1 - \frac{\rho bulk}{\rho teoric}\right) \times 100 \tag{7}$$

Where in eq. (6) and (7) $\rho teoric$ is the theoretical value of the sample, for eq. (6) $\rho apparent$ is the apparent density measure in eq. (4) and in eq. (7) $\rho bulk$ is the density measure in eq. (5). The total porosity englobes the infill porosity (created with the 3D printing process) and the actual bulk porosity in the sample, resulting in eq. (8) to calculate the infill porosity.

$$Infill\ porosity(\%) = \ Total\ porosity - \ Bulk\ porosity \tag{8}$$

3.7.2. Compression Test

To study and evaluate the mechanical properties of each geometry, compression tests were conducted. In this test, a universal testing machine from INSTRON was used, equipped with a 10 kN load cell and a speed of 0.5 mm/min. 10 samples from each geometry were tested. The samples were compared in terms of apparent compressive stiffness and ultimate compressive strength.

An important step taken before the mechanical testing was the removal of excess material left during printing. This step is crucial to ensure that the sample is as parallel as possible between the faces of the clamps. This alignment ensures that the material's surface is in full contact, allowing the test to yield the most accurate results possible. If there is any imbalance between the sides, the chances of early fractures and inconsistent results increases significantly. Subsequently, the same test was conducted on the three different concentrations of ZnO and MgO, using the same parameters and sample quantities.

3.7.3. Scanning Electron Microscopy

Unlike traditional optical microscopy, Scanning Electron Microscopy (SEM) utilizes a beam of electrons to obtain images of the surface of samples. This technique allows for better resolution at high magnifications compared to optical microscopy. However, it is important to note that this technique uses a highly energetic beam, where the primary electrons need to interact with the surface. In this work, the produced samples are predominantly ceramic, meaning they are non-conductive materials [48], [49]. Given this, it is necessary to prepare the samples in advance by coating them with a conductive material, such as gold-palladium alloy, which were used in this work.

For the analysis of the morphology of scaffolds with different geometries, the Hitachi S2400 SEM (Tokyo, Japan) was used. In the case of composite scaffolds with alterations in their formulation, the Phenom ProX G6 Desktop SEM (Massachusetts, USA) was utilized.

3.7.4. Energy Dispersive Spectroscopy

When the electron beam strikes the surface of the sample, the atoms within the sample become excited, undergoing electronic transitions. This process results in the production of highly energetic photons, also known as X-rays. The energy of these X-rays is unique to each element, which led to the implementation of an Energy Dispersive Spectroscopy (EDS) [48].

EDS is a technique that analyzes the X-rays emitted during SEM usage, extending beyond surface analysis to identify and quantify the elements present in the sample [49]. In this work, EDS was used to analyze the presence of the several elements in Hap-ZnO and Hap-MgO. The EDS analysis was conducted using the Phenom ProX G6 Desktop SEM (Massachusetts, USA).

3.7.5. Degradation test

In this task, the objective was to analyze the degradation rate of the material over a period of 5 weeks. Five samples of each type (Control and each of the HAp-ZnO and HAp-MgO composites) were submerged in Phosphate-Buffered Saline (PBS), placed in an incubator at 37ºC Celsius, and their weights were measured at the end of each week. In addition to measuring weight, the PBS was replaced every two weeks to ensure the stability of the experiment.

For the preparation of PBS, a 10x concentrated solution was used, which was then diluted with distilled water. To stabilize the pH at 7.4, a hydrochloric acid solution was employed to lower the pH as necessary. For the measuring, the samples are removed from the solution, the PBS inside is removed with air pressure and put in the oven in 60ºC for 5 hours. To calculate the degradation, Eq. (9) was used, employing the initial Pi (first day) and final Pt (after a given number of weeks) weights of each sample for the calculation.

$$Degradation\ Ratio\ (\%) = \frac{Pi - Pt}{Pi} \times 100 \tag{9}$$

Finally, one sample from each of the seven groups was selected, and SEM/EDS analysis was performed to study the morphological and chemical differences on the surfaces of the samples.

Chapter 4 - Scaffolds production and the effect of geometry

As previously mentioned, the scaffold's porosity plays a critical role in its development and production. By manipulating its design and geometry, it is possible to optimize scaffold's properties. Whether through CAD design, geometry creation based on mathematical formulas, or automatically generated geometries via slicing software, there are numerous possibilities for customizing design and creating functional geometries. Furthermore, it is essential to ensure that the chosen geometry not only fosters an environment conducive to bone regeneration but also provides sufficient structural integrity to withstand constant mechanical forces without deformation or fracture [7], [50].

This section presents the results leading to the formulation of the HAp base for robocasting, including particle analysis and rheology studies. It outlines how selected geometries were printed and the subsequent outcomes of all tests conducted to study the effect of geometry on mechanical performance, allowing for a comparative analysis between them.

4.1. Powders Characterization

Powders used in this work were analyzed using SEM/EDS. With this test at 3000x magnification, it was possible to observe that HAp and ZnO particles (Figure 9.a and 9.b) are more dispersed, with HAp particles showing minor agglomerations. In terms of size, HAp particles measure between 1 and 3 µm, while ZnO particles have an average size of 0.5 µm. For MgO, larger spherical agglomerations are observed, some reaching lengths of up to 100 µm. Figure 9.c shows MgO agglomerated particles in greater detail, with particle sizes ranging from 1 to 5 µm, most being around 2 µm. EDS results confirmed the presence of the constituent elements of each material, revealing a Ca/P ratio of 1.6 in the HAp particles, and the Zn and Mg were detected with no impurities.

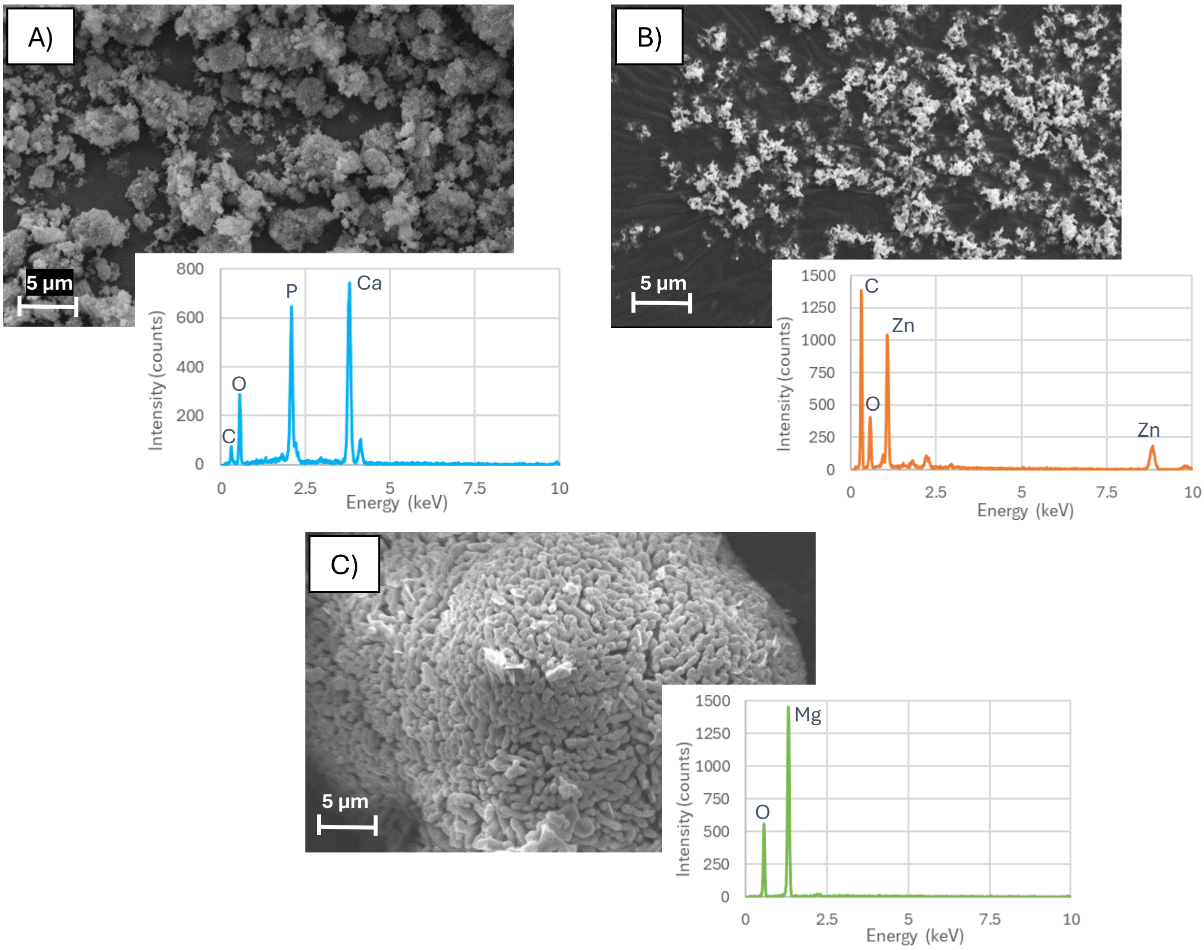

Figure 9 - SEM/EDS analysis of particles at 3000x magnification. A) HAp particles, B) ZnO particles, and C) MgO particles.

4.2. Paste Rheology

For paste (ink) production, as outlined in the methods, a rheometer was used to analyze viscosity in a range of shear rate. The initial solid content threshold reached was 40wt% of HAp, using only distilled water. Following this, the addition of dispersant to the mixture was investigated, yielding the results shown in Figure 10.

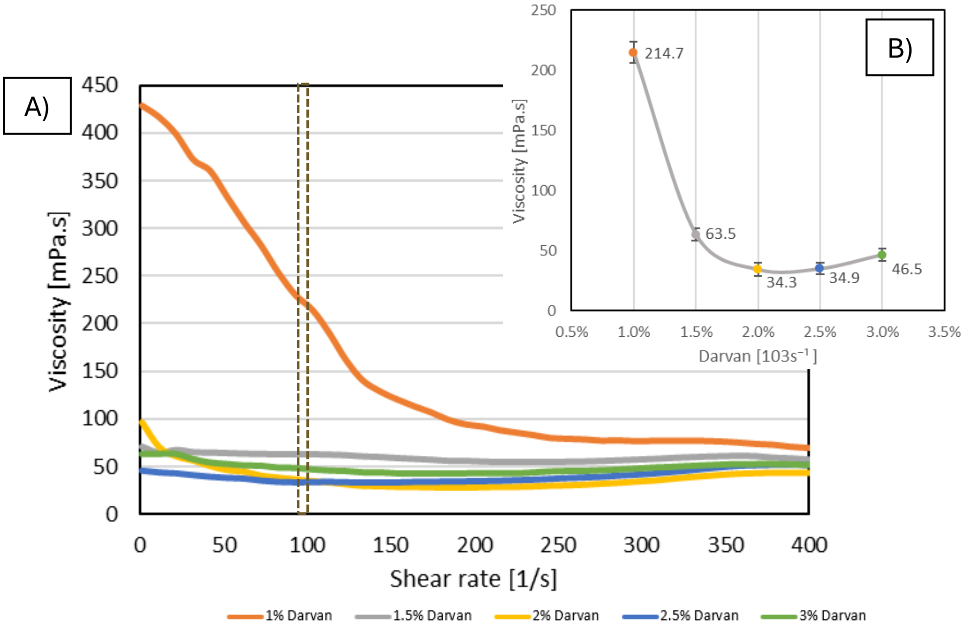

Figure 10 - Rheology paste with 40wt% HAp. A)influence of Darvan and B) values at 103 s^{-1}.

Analyzing the test, a decrease in viscosity with increasing Darvan concentration is clear. Taking into consideration the 3D printing parameters, the ceramic paste is subjected to a shear rate on 100 s^{-1} during extrusion. Based on this value, viscosities for each paste were determined near this level (103s^{-1}). Examining these points (Figure 10.B), the 2% and 2.5% Darvan samples displayed the lowest viscosity values (34.3 and 34.9 respectively). Generally, the samples show low viscosity; however, another factor to consider is that during mixture preparation, a high shear rate is applied, and with dispersant concentrations above 2%, viscosity starts increase a little from a shear rate of 100 s^{-1} onward. Thus, the 2% sample was chosen by having the lowest average viscosity throughout the test.

The next step involved a second increase in solids content using the selected dispersant concentration. Approximately 50wt% of HAp was achieved. However, initial tests showed that the dried samples were brittle, and many cracks formed during drying. To address this, sorbitol was added as a plasticizing agent. Filaments were then extruded using a syringe to observe their drying behavior (Figure 11). Among the different concentrations, the mixture with 5wt% sorbitol showed the best results, avoiding fractures during several rounds of extrusion. Another observation was the rapid drying of the paste, which negatively impacted layer bonding and its stabilization within the extruder. Consequently, PVA was added to the paste as a binding agent.

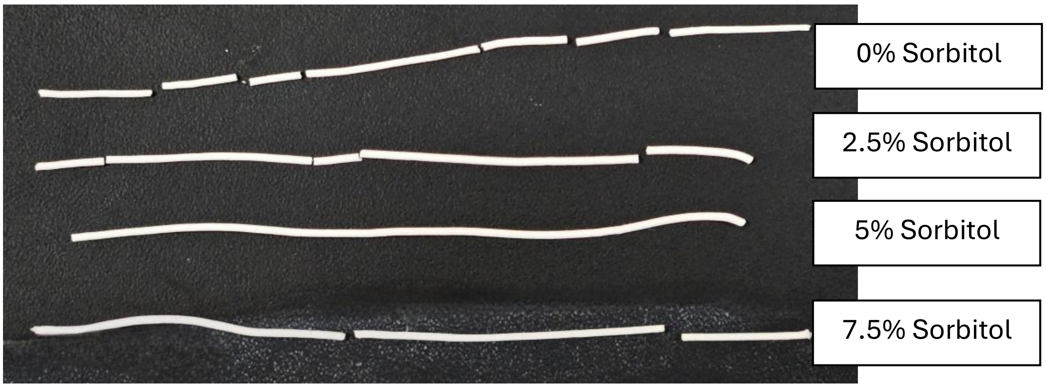

Figure 11 - Extrusion test with different concentrations of sorbitol.

To determine the ideal formulation of the paste with all the additives, a final viscosity test was conducted to identify the maximum content of HAp, as shown in Figure 12. The test was limited to 58 wt% of HAp, as the rheometer was not able to test more solid concentrations, marking the upper limit of this study. It is important to note that even though the viscosity increased with higher HAp percentages, all samples exhibited a pseudoplastic behavior, with viscosity consistently decreasing as the shear rate increased, regardless of the concentration of HAp.

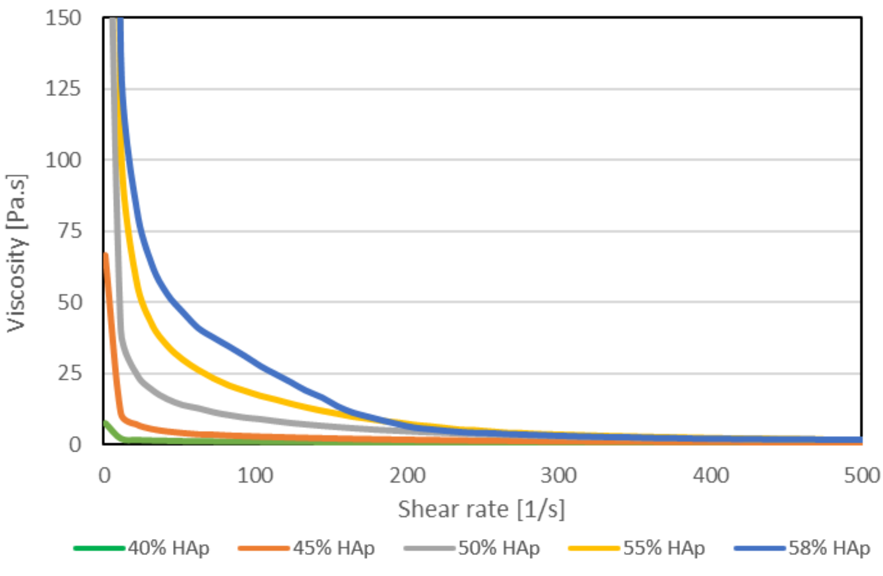

Figure 12 - Rheology analysis with the increase of HAp solid percentage.

4.3. Scaffolds

After producing the paste, samples with different geometry were printed, starting with simpler designs to test the printer's performance with the paste (Figures 13.A and 13.B). Following optimization, the printing proceeded with more complex geometries (Figures 13.C and 13.D).

Regarding their size after printing, the green bodies generally have an average size of 12.3 x 12.3 x 7.5 mm, which differs from the pre-selected dimensions of 12 x 12 x 8 mm in the slicer. During the printing process, the weight of the multiple layers caused the piece to slightly flatten and expand sideways.

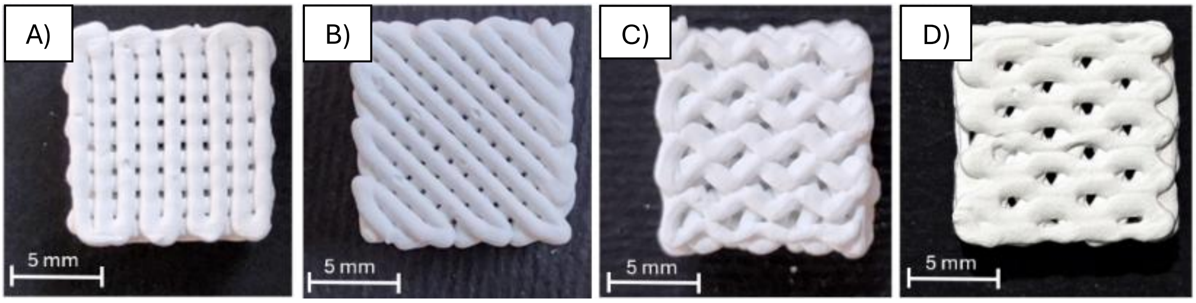

Figure 13 – HAp Scaffolds green bodies. A) Orthogonal, B) Diagonal, C) Gyroid and D) Honeycomb.

In some cases, small printing errors may occur, resulting in pieces with excess material on the surfaces (Figure 14.A). In these instances, before thermal treatment, the material is removed using sandpaper, and the parallelism of the piece is adjusted (Figure 14.B) to ensure the accuracy of the mechanical tests.

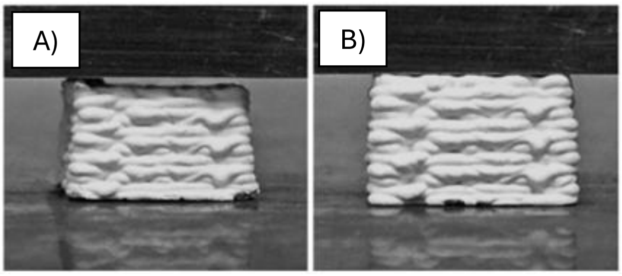

Figure 14 - Print error repair. A) before treatment and B) after treatment.

The thermal treatment of the samples was carried out. In Figure 15, we can observe the different geometries, highlighting their slight color change to a whitish-yellow and a reduction in size.

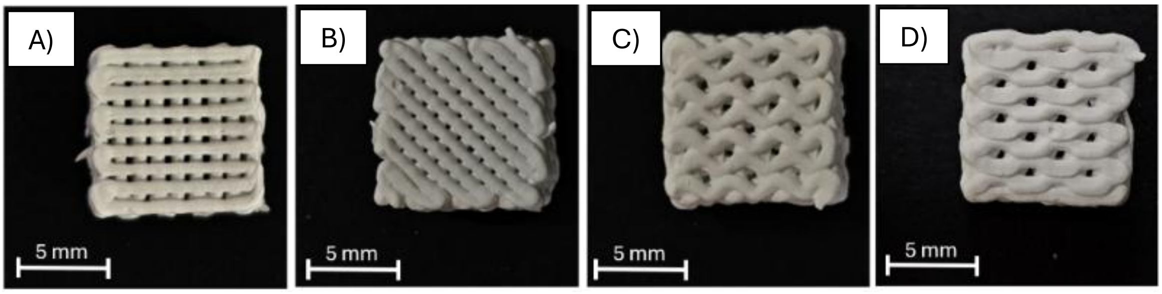

Figure 15 – HAp Scaffolds after thermal treatment. A) Orthogonal, B) Diagonal, C) Gyroid e D) Honeycomb.

4.3.1. Shrinkage, Density and Porosity

Regarding their size, the samples exhibited an average dimension of 10.4 x 10.4 x 6.6 mm, reflecting a volumetric reduction of nearly 40%, as shown in Figure 16.A. In terms of results, the Gyroid geometry demonstrated the smallest reduction (38.1 ± 1.7%), while the Orthogonal geometry experienced the most significant decrease (42.8 ± 1.0%). Additionally, the samples lost approximately 16% of their original weight (Figure 16.B), with the Gyroid geometry showing a lower average loss (15.6 ± 1.9%) compared to the Orthogonal geometry, which recorded a higher loss of 16.4 ± 0.4%.

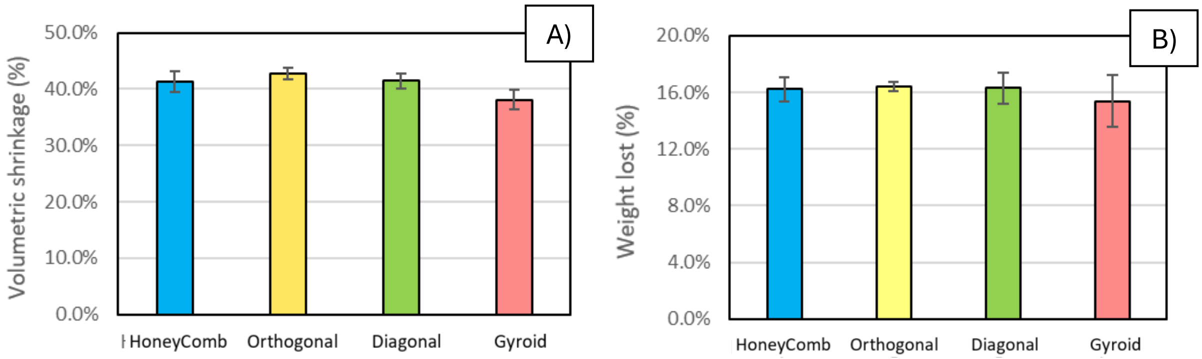

Figure 16 – HAp Scaffold's Shrinkage. A) Volumetric shrinkage and B) weight lost.

Next, calculations for density and porosity were conducted for each samples group. The samples exhibited an average density of 2.38 g/cm³, with a slight variation of ±0.02 g/cm³ between the geometries with the highest and lowest densities, specifically the Diagonal and Gyroid geometries, respectively. Additionally, the filaments produced from the paste after thermal treatment were measured, yielding a density of 2.5 ± 0.07 g/cm³. It is important to note that both the samples and the filaments have a density lower than the theoretical density of HAp, which is 3.17 g/cm³.

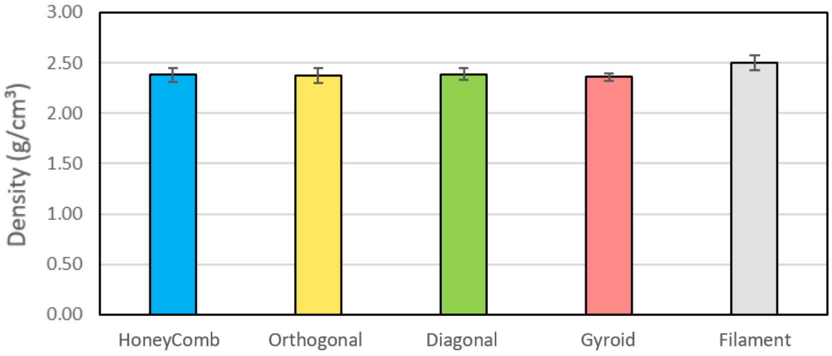

Figure 17 - HAp Scaffold's density after thermal treatment.

With these values, the porosity of each group was calculated (Figure 18). An average total porosity of 57 ± 1% was obtained. The infill porosity (porosity created with the 3D printing process), have an average of 33 ± 1% lower compared to the 50% original selected in the software. For compensation the filaments were not fully dense so there is porosity in the interior of the scaffold showing an average bulk porosity of 24 ± 0.6%.

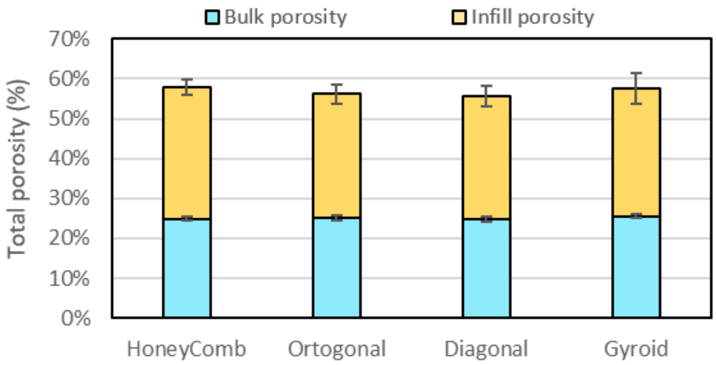

Figure 18 - HAp Scaffold's porosity of each geometry group.

4.4. Morphological analyses

For the morphological analysis of the samples, the SEM examination was divided into two parts: surface view (Figure 19 and 20) and lateral cross-section (Figure 21). Initially, in the surface observation at 20x magnification (Figure 19), it is evident how each group was printed. In the simpler geometries, the filaments did not remain perfectly straight, making the Orthogonal geometry displayed greater variation across the entire surface, with most pores measuring around 400µm, though some reached up to 700 µm. In contrast, the Diagonal geometry was the most compact, with surface pores smaller than 400 µm and some completely closed regions, illustrating an example of printing errors where extrusion exceeded the programmed amount.

In the more complex samples, variations in pore size can also be observed, with the Gyroid geometry showing the most pronounced differences. Gyroid samples exhibited large pore sizes, with some pores exceeding 1000µm in length. However, when assessing interlayer spacing, the pore size decreased to approximately 500µm. The Honeycomb geometry appears to be the most stable in terms of pore size throughout the entire sample. The pore sizes are similar to those of the gyroid geometry, with the surface pores being slightly smaller in size.

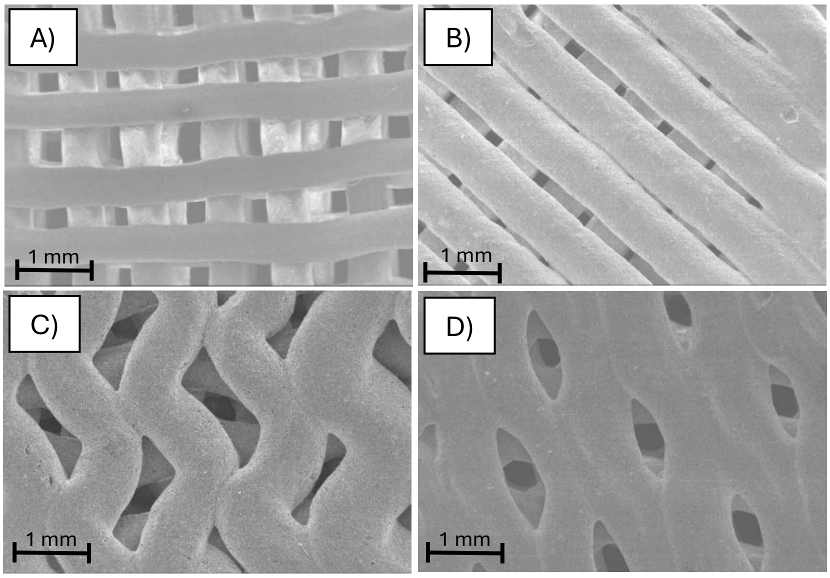

Figure 19 - HAp Scaffold's SEM analysis 20x. A) Orthogonal, B) Diagonal, C) Gyroid e D) Honeycomb.

Figure 20 shows the different porosities found in the produced scaffolds. When increasing the magnification from 20x to 100x, micropores on the surface formed by the air bubble porosity (Figure 20.B), which are similarly observed across all sample groups, with sizes the varies between 20-100 µm. Additionally, at a magnification of 3000x (Figure 20.C), the sintering porosity is visible, reaching sizes as small as 1 µm.

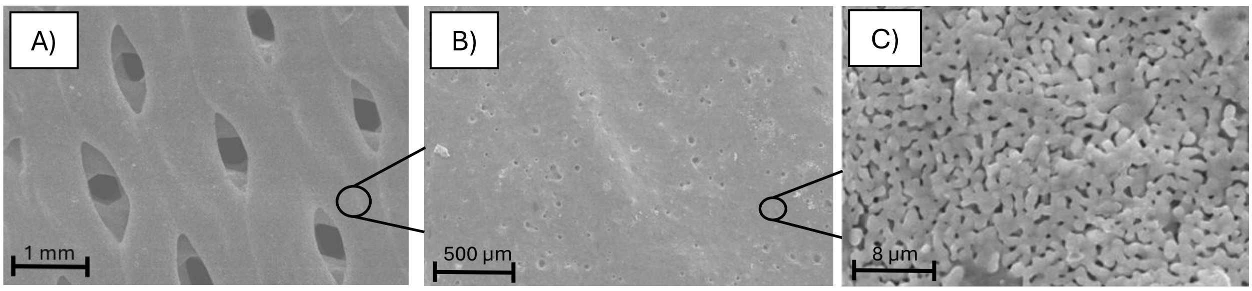

Figure 20 - HAp Scaffold's SEM Analysis. A)20x magnification, B) 100x magnification e C) 3000x magnification.

Using a resin mold a lateral cross-section as made of each sample, to analyze into the internal structure of each geometry (Figure 21). This view reveals multiple empty spaces/pores with no defined geometry through all samples, majority cause by the air bubbles inside the paste.

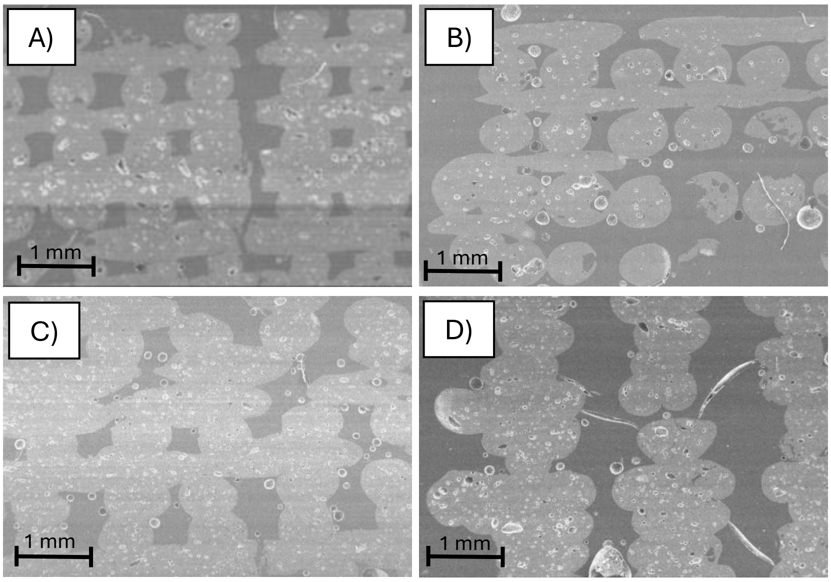

Figure 21 - HAp Scaffold's cross-section SEM low magnification analysis. A) Orthogonal, B) Diagonal, C) Gyroid e D) Honeycomb.

Figure 22 further enhances our observation by providing a detailed view of the air bubble porosity within the sample (Figure 22.A), where the pores are dispersed randomly and vary in size (20-150 μm). Smaller pores (Figure 22.B) display a similar structure to those seen on the SEM surface image (Figure 20.C); however, they are less distinct due to the presence of resin between them.

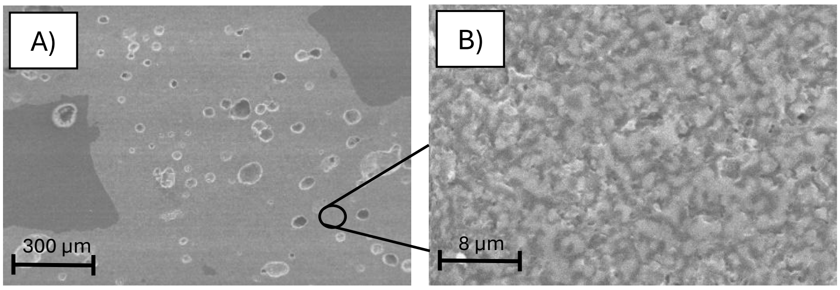

Figure 22 - HAp Scaffold's cross-section SEM high magnification analysis. A) 50x magnification and B) 3000x magnification.

4.5. Compressive test

To conclude the study on the influence of geometry on the mechanical properties, a compression test was performed for each group (Figure 23). In terms of results, the Honeycomb and Diagonal geometries exhibited a more consistent stress-strain curve compared to the other groups, which displayed multiple fractures throughout the tests before reaching their maximum stress point (Figure 23.A). Overall, in most tests, the peak stress was reached at an average strain of 0.05.

A statistical comparison of the maximum stress results from the compression test (Figure 23.B) shows that the Honeycomb geometry group recorded the highest average value at 15.7 ± 1.4 MPa, outperforming the other groups. The Gyroid geometry registered the lowest average value, 10.4 ± 3.1 MPa, and displayed the highest variance within its group. The Diagonal and Orthogonal geometries had relatively similar results, with Diagonal samples recording slightly higher values at 12.2 ± 1.8 MPa compared to Orthogonal samples at 11.9 ± 2.3 MPa.

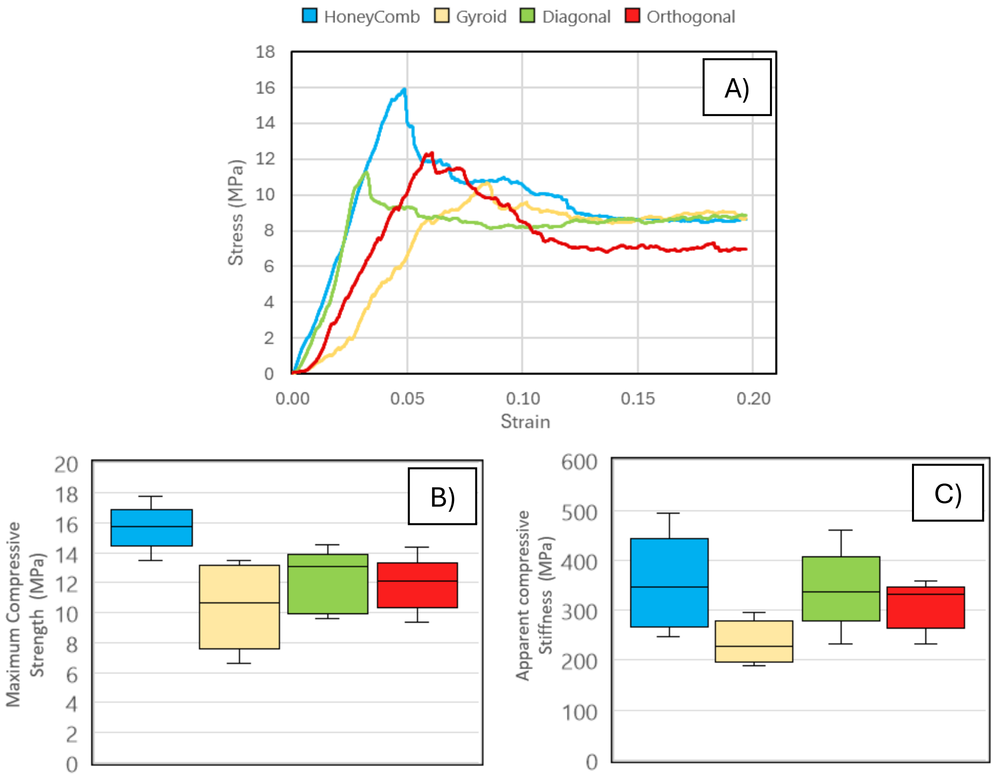

Figure 23 - HAp Scaffold's Compressive test. A) Compressive curve, B) maximum compressive strength and C) Apparent compressive Stiffness.

Finally, the apparent compressive stiffness of the different geometries (Figure 23.C), orthogonal and gyroid and the lowest values, with an average value of 311 ± 68 and 235 ± 44 MPa respectively. And the diagonal and Honeycomb have the highest with 341 ± 107 and 350 ± 143 MPa respectively. Based on all the results obtained, the Honeycomb geometry was selected as the base structure and will be used in the various formulations with ZnO and MgO developed in the following steps.

4.6. Result discussion

Regarding the production of the HAp pastes, Figure 10 shows the influence of Darvan over the past rheology. The choice of the 2wt% dispersant formulation was based on its lower viscosity throughout the entire test. All pastes had a pseudoplastic behavior through the applied shear rate range, making it even more adequate for the printing process [23],[27].

For print optimization (Figure 12), the maximum possible concentration was used, achieving successful printing up to 58wt%. By identifying the printer's theoretical shear rate and the paste corresponding viscosity, it was observed that, at 100 s^{-1}, the paste's viscosity registered an average value of 27.5 ± 3.5 Pa.s. According to studies such as that of Shao et al., viscosities at 100 s^{-1} vary depending on concentration, ranging from 17 Pa.s to 42 Pa.s. Although printer settings and paste formulations are obviously different, it is worth noting that a higher-viscosity paste was used in these authors study, compared to the one produced in this work [51].

After printing scaffolds with different geometries, a few key points should be highlighted. During printing, there were several instances where material extrusion rate was not uniform. This could be due to accumulated pressure in the syringe, processor error, paste drying in the extrusion nozzle, or even some poorly homogenized paste. Such issues result in a non-uniform layer, which may exhibit a more open porosity than expected or have pores that are completely covered. This have been reported as limitation by several authors [23], [52], [53].

Due to extrusion not being fully controllable, there was excessive material extrusion, as evidenced by the porosity of the samples. It was observed that the infill average porosity was nearly 13% lower than intended (50%) (Figure 18). Through the density calculation and SEM imaging (Figure 19 and 20), there's a formation of air bubble and sintering porosity, increasing the overall porosity. At magnification 100x (figure 20) allowed for the observation of various mesopores, ranging from 20 to 100 μm in size, cause by the air bubble in the paste. This feature is even more evident when viewing the lateral cross-sections of the scaffolds (Figure 21), where pores of these dimensions are present internally. At higher magnifications, sintering porosity is visible with approximately 1 μm, and in some cases up to 2 μm. In the cross-sectional view, is noted the presence of resin within the sintering porosity, showing that is an interconnection structure.

As noted in the literature, each level of porosity contributes to different aspects of bone regeneration. Macropores, directly formed by the printing process, support the formation of new blood vessels and the infiltration of cells and nutrients throughout the scaffold. Mesopores (air bubble porosity) facilitate cell migration into the scaffold, while micropores (sintering porosity) promote cell adhesion and protein retention [11], [12], [54].

Temperature and sintering time are crucial for the densification of HAp. According to Trzaskowska et al. and Muralithran et al., sintering porosity can lower to 5% when subjected to a temperature of 1250°C. and obtained similar morphology to the one obtained in the present work for a sintering temperature of 1150ºC. [55], [56]. This can be due to differences in the powder size distribution or densification during the fabrication of the green body.

In terms of compression test results (Figure 23), the Honeycomb geometry stands out, with a value more than 30% higher compared to the averages of the other geometries. When compared to characterization or the morphology of the scaffolds, all geometries have overall similar values. Having only one test that the Honeycomb stands out. So, one point to consider in the geometry selection process was the finite element studies, which analyzed the Honeycomb structure compared to other geometries [57], [58], [59]. Through this analysis, the authors concluded that the Honeycomb structure exhibits superior properties, and more weight distribution compared to the other applied geometries, being compared not only to simple geometries such as the orthogonal but also to more complex geometries [58], [59].

In a study by Shao H. et al., where scaffolds with different geometries were printed and mechanical tested, it was shown as well that the Honeycomb geometry stood out for both its compressive strength and its elasticity modulus, being twice as strong as the group using a rectangular geometry (equivalent to the Orthogonal geometry in this work) [60]. This highlights how the Honeycomb geometry excels in the production of scaffolds. Finally, when compared to the test results of HAp scaffolds, Shao et al. recorded an average value of 17 MPa, which is similar to the values of the Honeycomb in this work (average value of 15.7 MPa). However, in the study, sintering was carried out at 1200°C, which directly influences the mechanical properties [51].

Chapter 5 - HAp-ZnO Scaffolds

Following the development of the HAp-based formulation, the evaluation of various geometries, and the selection of the primary design, the next step was to identify methods to enhance the base properties of HAp. As discussed in Chapter 2 and in numerous studies such as Ielo et at. and Saxena et al., HAp exhibits limitations in certain mechanical and biological properties. Literature suggests that the addition of ZnO particles to HAp may improve the mechanical properties of scaffolds while also contributing to tissue regeneration through its antibacterial effects [39], [45].

For this reason, ZnO particles were incorporated into the scaffold formulation at varying concentrations to investigate their impact on both mechanical properties and *in vitro* PBS degradation tests. In this section, all tests from the previous chapter were conducted similarly, with the addition of a degradation test in a PBS environment and SEM/EDS analyses. A discussion is included at the end to summarize all findings and to assess how the amount of ZnO affects scaffold properties across each formulation.

5.1. Rheology

As in section 4.1, the first step involves studying the rheology of the different ZnO formulations to determine whether it is possible to modify the formulation by slightly reducing the HAp content while adding ZnO. As shown in Figure 24.A, the ZnO formulations exhibit lower viscosity, when compared to the control up to a shear rate of 150 s^{-1}. Among the ZnO formulations, the 2.5wt% variant demonstrates the lowest viscosity within the group. The apparent viscosity values of each paste used during the extrusion are presented in Figure 24.B.

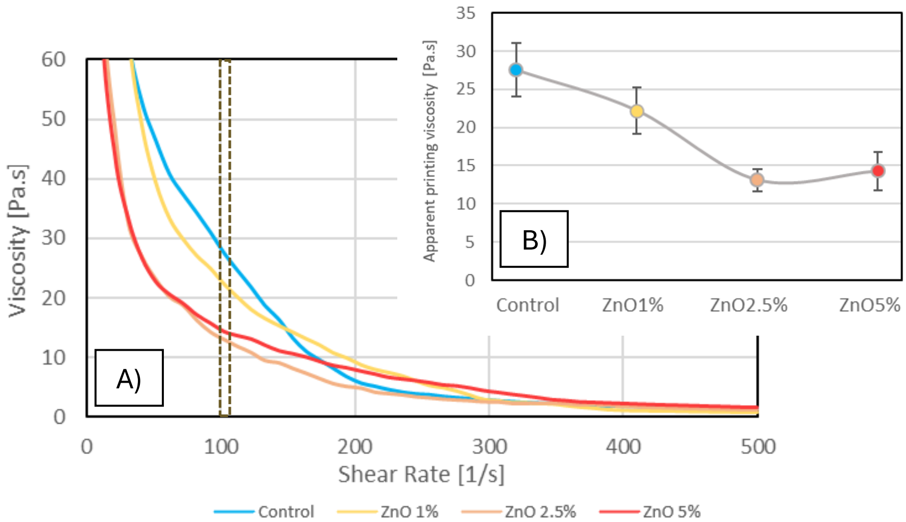

Figure 24 - Rheology test of HAp-ZnO pastes. A) Viscosity-shear rate curve and B) Apparent printing viscosity.

5.2. Scaffolds

A noticeable difference between the control sample and the HAp-ZnO composites is their color, which becomes evident only after sintering. As seen in Figure 25, the ZnO sample appears whiter compared to the samples shown in section 4.1.3 after printing. However, they also exhibit a slight bluish tint, a characteristic observed in all samples, regardless of the wt% of ZnO present in each formulation.

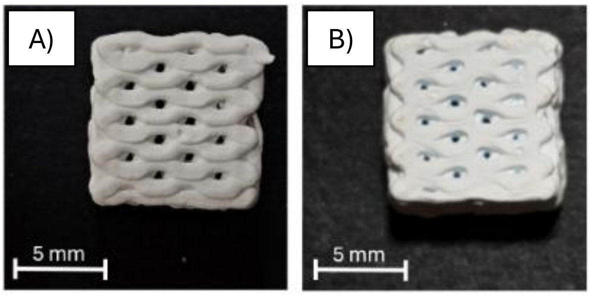

Figure 25 - HAp-ZnO Scaffolds after thermal treatment. A) HAp and B) HAp-ZnO.

5.2.1. Shrinkage, Density and Porosity

Regarding their size, the HAp-ZnO composite have an average dimension of 10.2 x 10.2 x 6.2 mm, resulting in an average volumetric reduction of approximately 41.8%. In terms of results (Figure 26.A), the samples with 2.5wt% and 5wt% exhibit the greatest reductions (43.2 ± 2.1% and 42.5 ± 2.8%, respectively), while the 1wt% sample shows the smallest average decrease at 39.6 ± 1.4%.

Concerning their weight (Figure 26.B), the 1wt% samples lost the same amount of weight as the control samples (16.2 ± 0.8%). It's important to note that as the ZnO concentration increased, the samples exhibited a lower weight reduction, losing only 13.1 ± 2.2% average weight for the ZnO 5wt% samples, which is 3% less than the control sample.

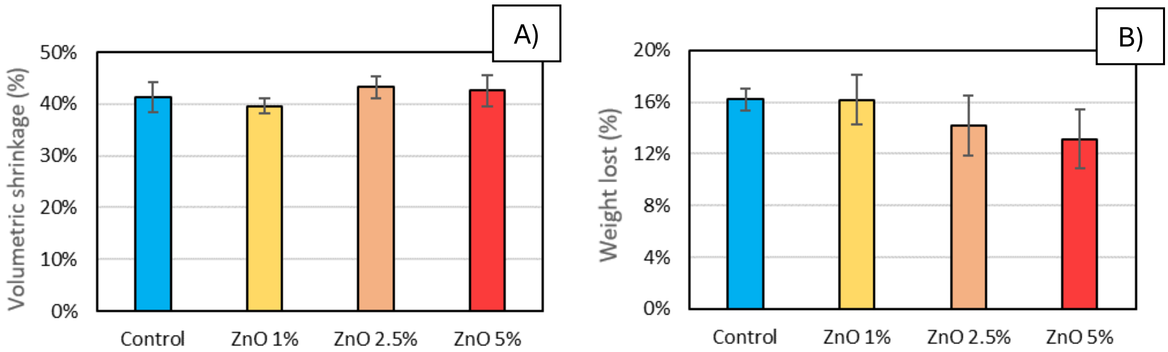

Figure 26 - HAp-ZnO Scaffold's shrinkage. A) Volumetric shrinkage and B) weight lost.

Next, the density of the different formulations was calculated. In Figure 27, an increase in density is observed as the amount of ZnO rises. The group with 5wt% recorded an average density of 2.55 ± 0.07 g/cm³, which is approximately 7% higher than the density of the control sample (2.38 ± 0.02 g/cm³). However, it remains lower than the theoretical density of HAp (3.17 g/cm³) and if add in consideration the addition of ZnO, the maximum theoretical density of HAp-ZnO should be 3.29 g/cm³.

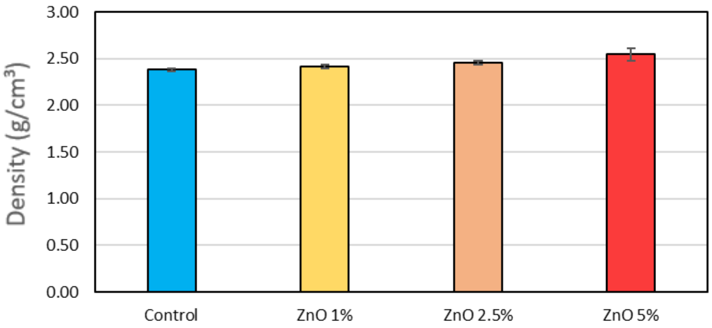

Figure 27 - HAp-ZnO Scaffold's density after thermal treatment.

Regarding the porosity of the HAp-ZnO samples, values are lower than those of the control samples (Figure 28). Samples with 1wt% exhibit the same average total porosity and pores porosity as the control sample. In contrast, the samples with 2.5wt% and 5wt% show a decrease to 56.5 ± 1.7% and 55.6 ± 2% of total porosity, with both infill and bulk porosity decreasing evenly in both groups.

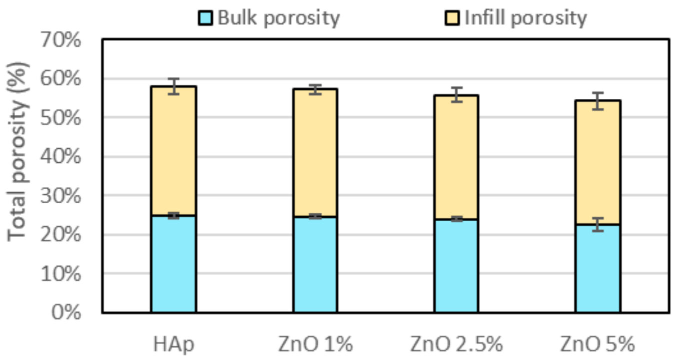

Figure 28 - HAp-ZnO Scaffold's Porosity.

5.3. Microstructural analyses

When analyzing the surface of the samples using SEM (Figure 29), the HAp-ZnO composites show a reduction in both the quantity and size of the micropores present. This difference is more pronounced in the 2.5wt% sample (Figure 29.C) and the 5wt% sample (Figure 29.D), where there is even a loss of interconnectivity among the micropores that is visible in the control sample (Figure 29.A) and in the 1wt% ZnO sample (Figure 29.B). It is important to the air bubbles porosity observed in Figure 29.A and C are present in all samples, regardless of the formulation.

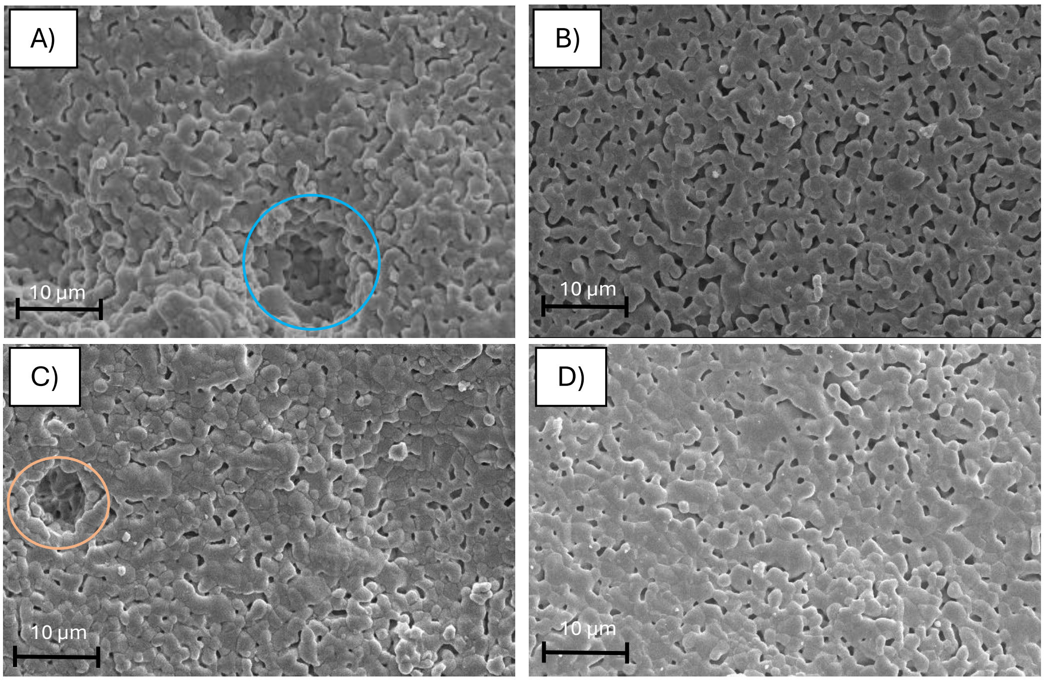

Figure 29 - HAp-ZnO Scaffold's SEM at 50x magnification. A) HAp , B) ZnO 1%, c) ZnO 2.5% and D) ZnO 5%.

EDS analysis was conducted on each HAp-ZnO composite (Figure 30). First, the 1wt% sample was examined (Figure 30.A), where a low quantity of Zn was detected in the various EDS analyses performed. Even in regions that could be visually identified as zinc particles (as illustrated in Figure 30.C), there was only a minimal amount of Zn present. For the 2.5wt% sample (Figure 30.B), similar findings were observed, with only a slight increase in zinc content. Additionally, the figure (Figure 30.B) highlights the previously mentioned micropores, which show a noticeable reduction when viewed at a higher magnification.

Lastly, the EDS analysis of the 5wt% ZnO (Figure 30.C) sample revealed the presence of ZnO particles, as indicated by the prominent zinc peak in the graph of Figure 30.C. On its surface, an increase in the interconnectivity between particles is noted; however, like in the previous samples, the quantity of ZnO remains low.

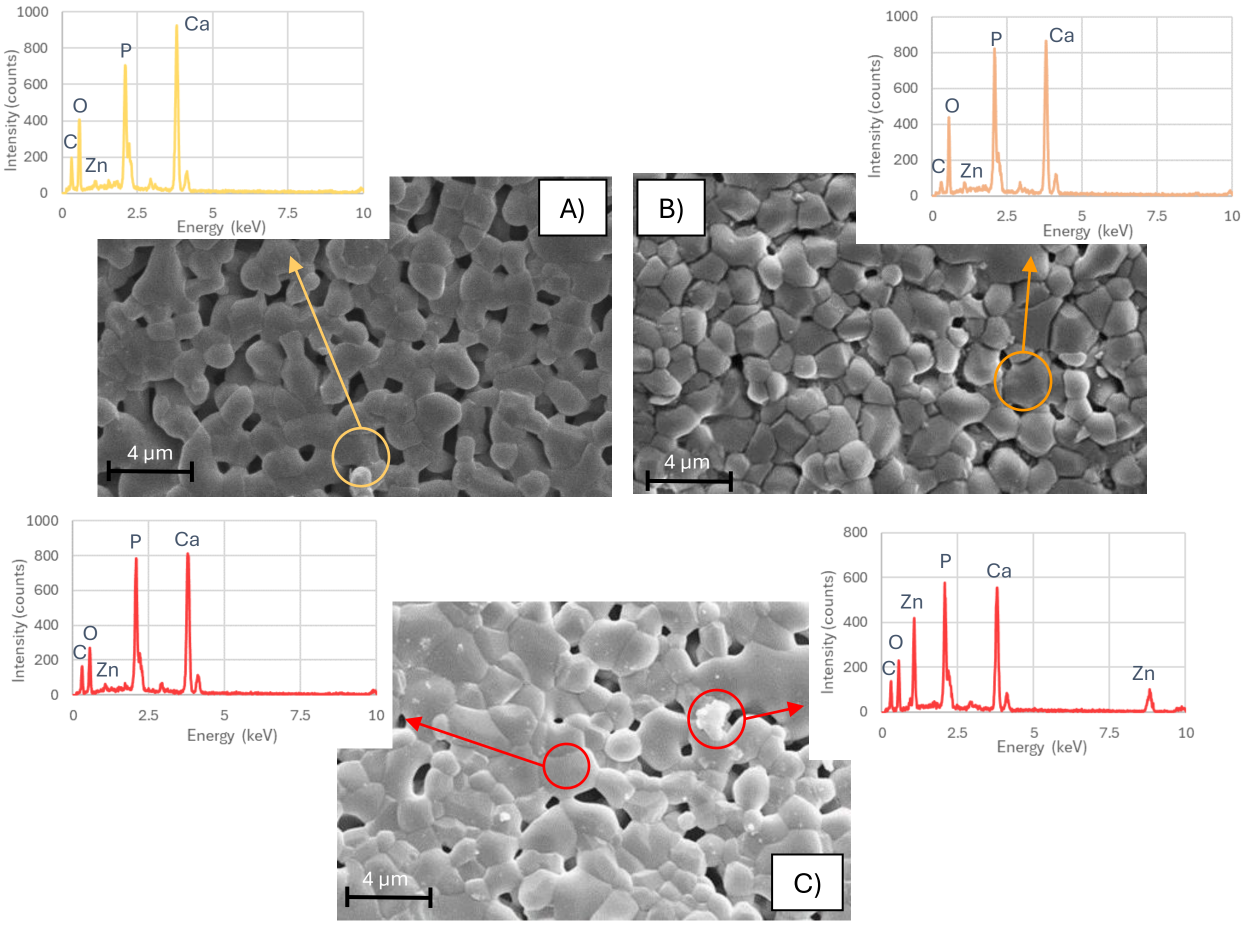

Figure 30 - HAp-ZnO Scaffold's SEM/EDS at 5000x magnification. A) ZnO 1%, B) ZnO 2.5% and C) ZnO 5%.

5.4. Compressive test

Analyzing the mechanical behavior of HAp-ZnO composites through the compression tests (Figure 31.A), an increase in maximum compressive strength is observed with the rising percentage of ZnO, reaching a maximum value of 37 MPa in the 5wt% ZnO group. However, despite these higher stress values, Figure 31.B shows that the variation in maximum values obtained from each group increases starting from the 2.5wt% ZnO group. No significant differences were found between the control and the 1wt% ZnO samples.

Evaluating the apparent compressive stiffness (Figure 31.C), a similar trend is observed, with an exponential growth corresponding to the increase in ZnO percentage. The HAp samples measure an average value of 350MPa, while the average apparent compressive stiffness for the 5 wt% ZnO group reaches 792MPa. In this case, the variation in average values among the groups is comparable.

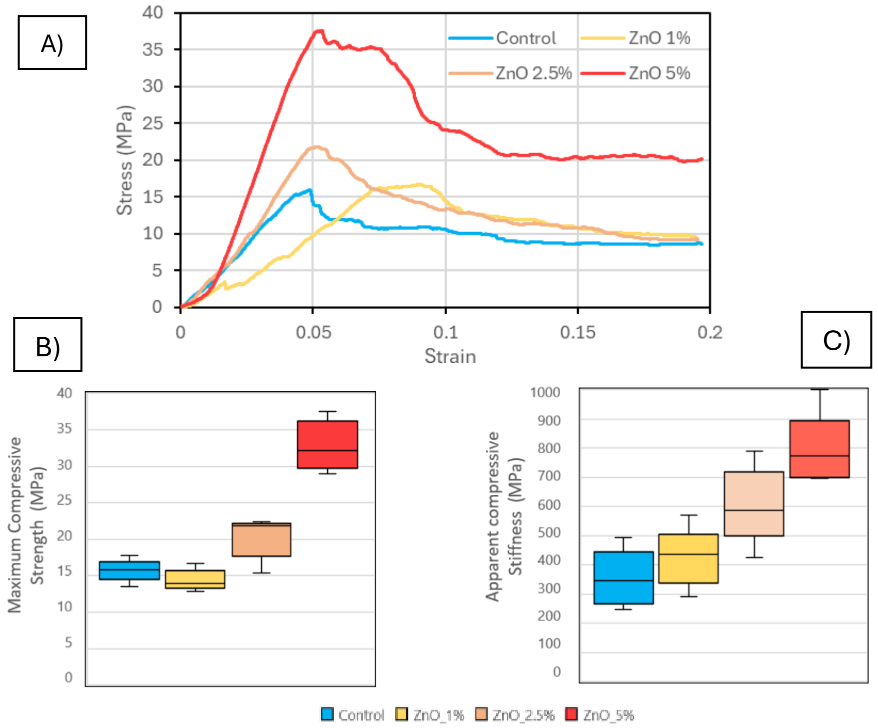

Figure 31 - HAp-ZnO Scaffold's compressive Stress. A) Compression curve, B) Maximum stress and C) maximum compression stiffness.

5.5. Degradation test

The degradation test results are given in figure 32. Over the course of five weeks, the HAp sample recorded a weight loss of approximately 0.6%. In contrast, the 1wt% ZnO sample exhibited a minimal loss of just 0.1%. Furthermore, the composites with 2.5wt% and 5wt% ZnO showed an increase in weight compared to their original weight, with the 5wt% ZnO approaching an increase of nearly 1%.

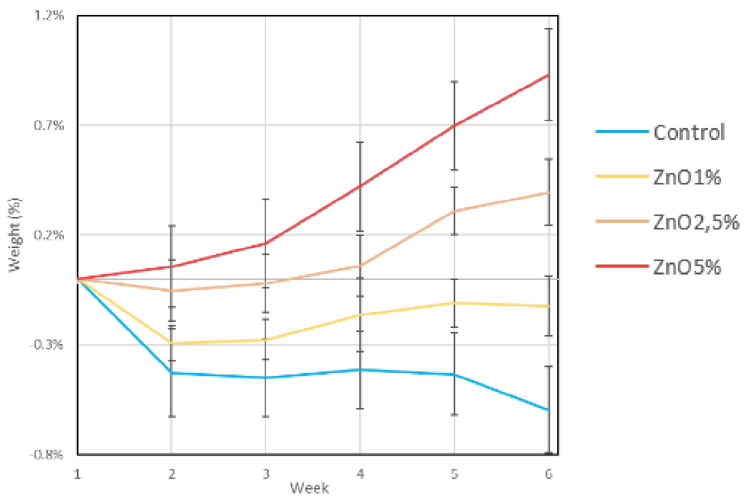

Figure 32 - HAp-ZnO Scaffold's degradation test.

After five weeks in PBS the samples in Figure 33 were analyzed by SEM. At a magnification of 100x, the HAp sample (Figure 33.A) displays higher microporosity compared to the HAp-ZnO samples (Figures 33.B to 33.D). Notably, the surface of the ZnO composites shows the formation of particles, with this effect being most pronounced in the scaffold with the highest percentage of ZnO (Figure 33.D).

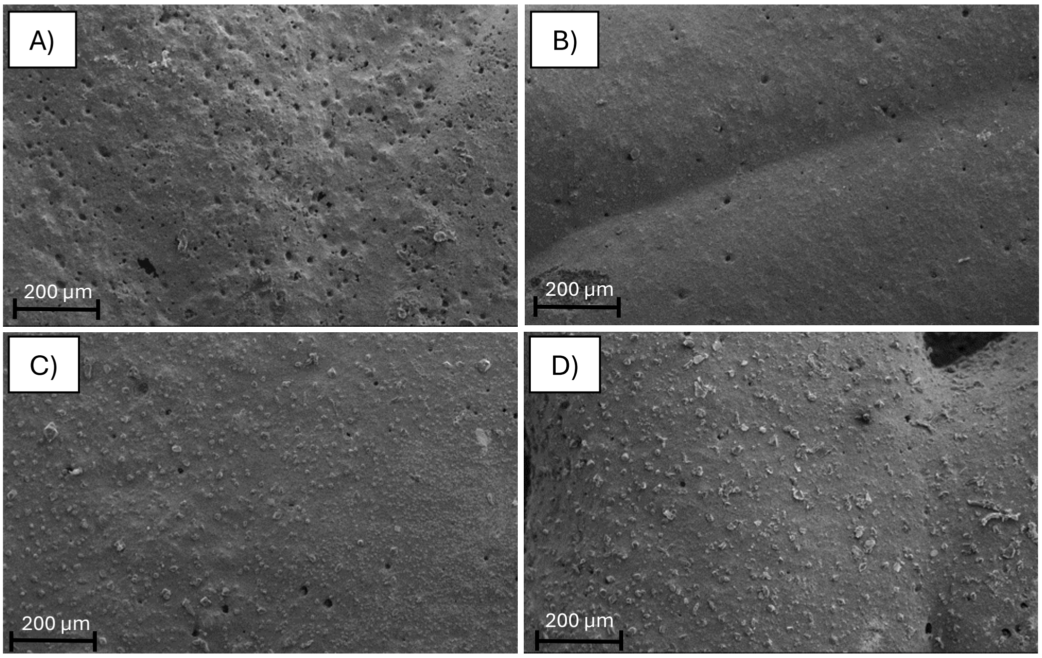

Figure 33 - HAp-ZnO Scaffold's SEM after degradation test. A) HAp, B) ZnO 1%, c) ZnO 2.5% and D) ZnO 5%.

To study the chemical modifications induced by PBS exposure, EDS analysis was performed. In Figure 34.A, the control sample shows minimal elemental changes, displaying primarily physical alterations. For the sample with 1wt% ZnO (Figure 34.B), small crystalline formations are observed, which EDS confirms to contain zinc, although they lack a consistent geometry, with both rectangular and rounded shapes appearing. Additionally, these zinc regions show a reduction in Ca.

With the increase in ZnO content, the 2.5wt% sample (Figure 34.C) not only displays zinc particles but also the initial formations of crystals with presence of zinc, oxygen (O) and phosphate. The content recorded across all EDS scans indicates that these particles and crystals likely form by the ZnO release from the composite and the phosphate within the PBS solution. Finally, in the 5wt% ZnO sample (Figure 34.D), an increase in the formation of zinc phosphate crystals is observed. Analysis of the PBS samples further reveals that most of the surface does not contain zinc, as highlighted in the secondary analysis shown in Figure 34.D, concentrating only on the crystal formation.

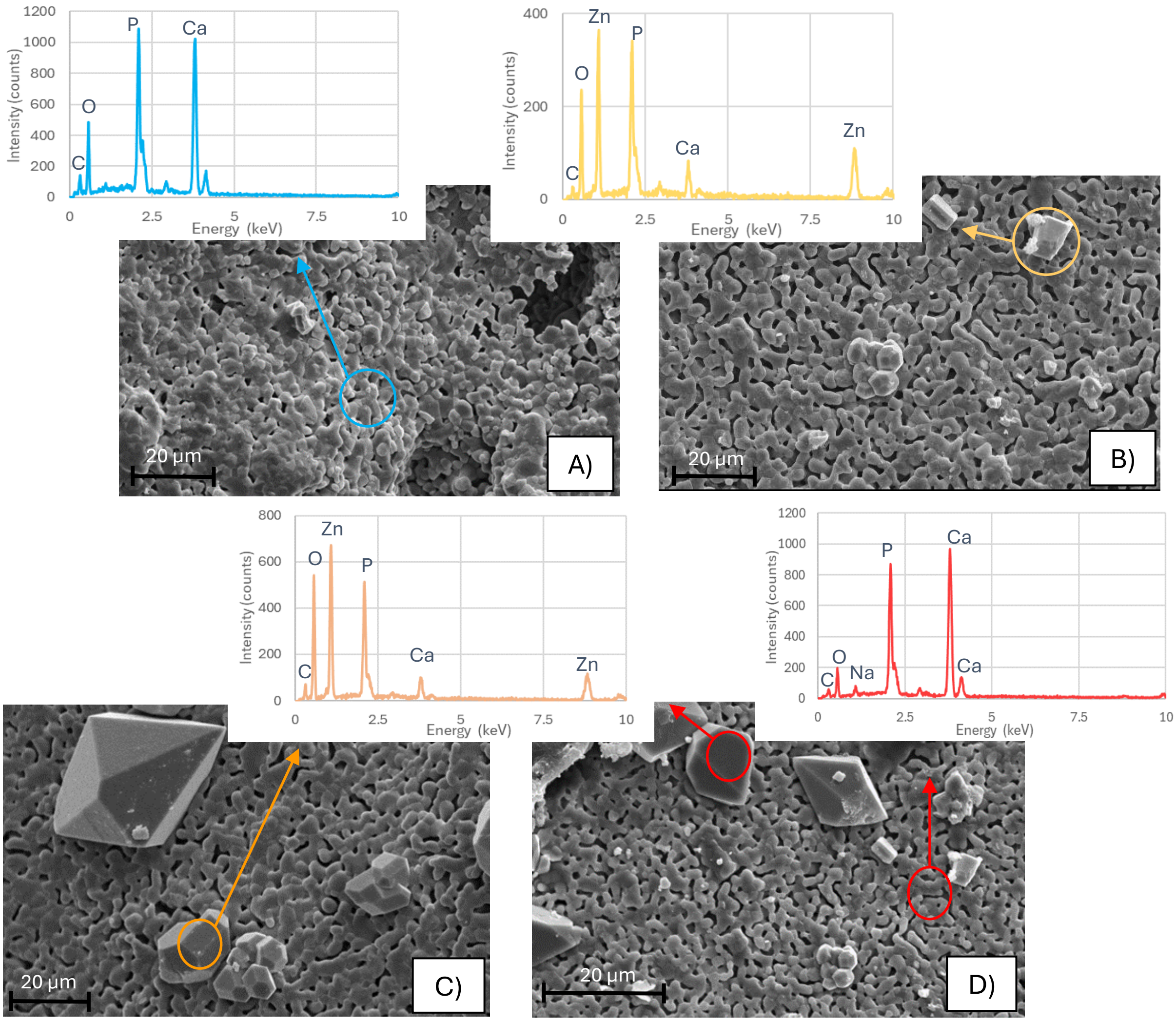

Figure 34 - SEM/EDS of the HAp-ZnO. A) HAp (2000x), (B) ZnO 1% (2000x), C) ZnO 2.5% (2000x) and D) ZnO 5% (1000x).

5.6. Discussion of the incorporation of ZnO

Starting with the rheological study of ZnO incorporation (Figure 24), it is evident that as more ZnO is incorporated, the paste becomes less viscous. This is particularly noticeable at lower shear rates, including within the 3D printing range (100 s^{-1}), where the control sample is 1.5 times more viscous than the 2.5 wt% and 5 wt% samples. One of the key reasons for this is the particle size, as shown in Figure 9, where one can see that ZnO particles are smaller than HAp ones. Additionally, ZnO particles are much denser (5.61 g/cm^3) compared to HAp particles (3.17 g/cm^3). As ZnO is incorporated by weight percentage, this results in a higher volumetric proportion of HAp to ZnO. This leads to the paste being less viscous.

Regarding the characterization of the HAp-ZnO samples compared to the HAp samples show less volume, resulting in an increase in density and, consequently, a reduction in porosity. Correlating this information with the SEM/EDS analysis (Figure 29 and 30), a reduction in the microporosity of the HAp-ZnO scaffolds is evident, where, as the ZnO content increases, the microporosity becomes more closed. This indicates that ZnO accelerates densification without the need to increase the sintering temperature. Furthermore, the consistently low amount of visible isolated ZnO particles found across almost the entire surface and the detection of Zn ions show the ZnO particles were well mixture during the paste production.

In a study by Naqshbandi et al., where HAp scaffolds were produced with Zn, it was shown that increasing the amount of Zn in the scaffolds as the same effect leading to an increase in their apparent density and, consequently, a decrease in porosity, with a reduction of up to 8% in the original porosity. Additionally, the SEM analysis conducted demonstrate that as the Zn content increased, the micropores became more closed [61].

Through the compression mechanical test, as shown in Figure 31, we can observe how the densification of the HAp-ZnO samples influenced the increase in maximum stress and apparent compressive stiffness when compared to pure HAp. The results show 2 times increase compared to the control group with only 5wt% of ZnO.

According to Mazaheri et al., the sintering of ZnO has the ability to achieve high density without undergoing phase transformations up to 1300°C. It is noted that, in some cases, it can reach a densification rate of 95% when sintered at temperatures above 1100°C. As previously mentioned, HAp also undergoes sintering at similar temperatures, and even slightly higher ones (95% at 1250°C). This demonstrates the compatibility, at least in terms of temperature and sintering conditions, between the two materials [56], [62].

Analyzing the initial degradation tests (Figure 32), it was observed that over 6 weeks, as the sample concentration of ZnO increased, the weight loss decreased, with the samples containing 2.5wt% and 5wt% even showing a weight gain. This factor can be explained by the SEM/EDS analysis, where the formation of ZnO crystals is visible. These crystals are rich in Zn, P, and O. Since HAp is naturally difficult to degrade, as confirmed by reviews from Lelo et al. and Panda et al., only a 0.6% loss was observed after 6 weeks [37], [39]. Thus, it is possible to highlight that the ZnO present in the scaffolds interacted with the P in the PBS, forming these crystals, probably of zinc phosphate which resulted in a weight increase that exceeded the HAp loss from the scaffold.

Chapter 6 - HAp-MgO Scaffolds

To further investigate the properties of HAp scaffolds, the incorporation of MgO particles were examined. MgO is recognized for enhancing various scaffold properties, especially by improving biological performance and significantly accelerating bone regeneration. This integration into HAp scaffolds has shown promising effects like as said in the literature review by promoting cellular responses crucial to osteointegration, which is essential for successful bone healing [40], [42], [43].

This chapter closely mirrors the previous one, with the primary distinction being the material incorporated into the scaffold structure. Focusing on analyzing how increased MgO concentration on the HAp-MgO scaffolds influences the mechanical properties and the behavior in a PBS environment.

6.1. Rheology

Proceeding with the rheology analysis of HAp-MgO pastes, Figure 35 shows that MgO containing formulations generally exhibit higher viscosity than the HAp up to a shear rate of 300s^{-1}. The 1wt% MgO paste is the only one with a lower viscosity than the base formulation. It is worth noting that MgO particles did not dissolve as readily in distilled water compared to ZnO particles, which may partly explain the viscosity increase observed with higher MgO concentrations. Shear rate values used for printing these formulations are shown in Figure 35.B, illustrating the trend of increased viscosity corresponding to higher MgO percentages.

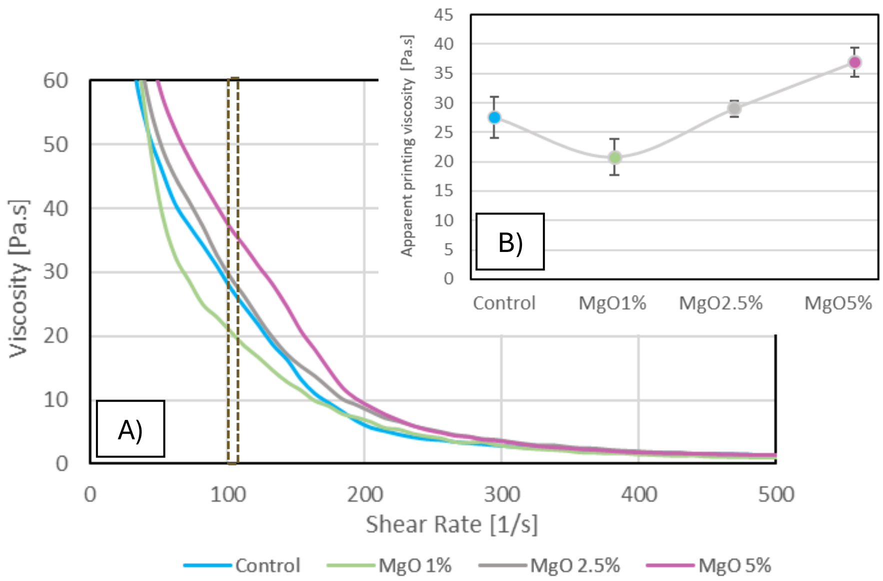

Figure 35 - Rheology analysis of HAp-MgO pastes. A) Rheology curves and B) Apparent Printing viscosity.

6.2. Scaffolds

Regarding the HAp-MgO scaffolds (Figure 36), no significant physical changes were observed post-sintering compared to the control samples. In terms of color, some samples appeared slightly lighter than the HAp samples, though this variation was not consistent across all HAp-MgO samples.

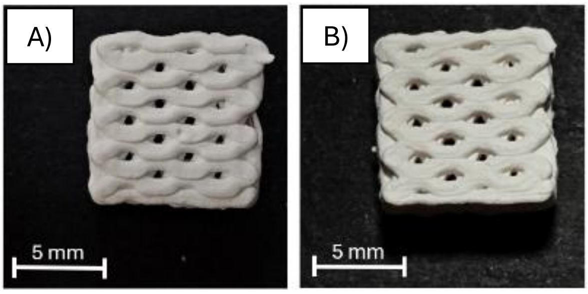

Figure 36 - HAp-MgO Scaffolds after thermal treatment. A) HAp and B) HAp-MgO.

6.2.1. Shrinkage, Density and Porosity

In terms of shrinkage during thermal treatment, the HAp-MgO samples reached an average size of 10.5 x 10.4 x 6.5 mm, showing an average volumetric reduction of around 32.2%. As shown in Figure 37.A, the 2.5wt% and 5wt% MgO exhibited the smallest reduction, with volumetric contractions of 30.1 ± 2.6% and 28.6 ± 3%, respectively. In contrast, the 1 wt% MgO sample showed a reduction of 37.7 ± 1.8%, more similar to the control samples average volumetric reduction of 41.4 ± 2.8%. Regarding weight loss (Figure 37.B), the HAp-MgO samples lost slightly more mass than the HAp, with an average increase in weight reduction of about 1.1%. The 1 wt% samples lost an average of 17 ± 0.4% of their original weight, while both the 2.5 wt% and 5 wt% samples lost an average of 17.5 ± 0.7%.

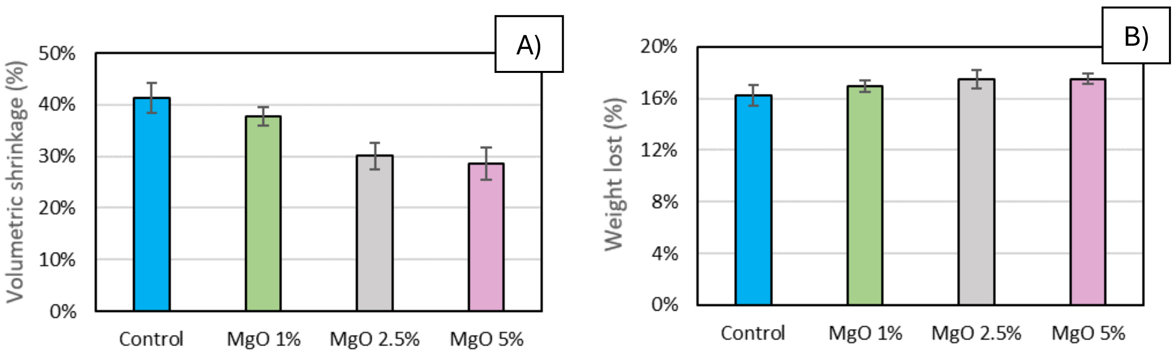

Figure 37 - HAp-MgO Scaffold's Shrinkage. A) Volumetric shrinkage and B) weight lost.

In terms of density for the HAp-MgO composites, Figure 38 reveals a slight decrease in density with increasing MgO content. The 1wt% MgO group maintained the same density as the control group, while the 2.5wt% MgO composites showed an average decrease to 2.34 ± 0.02 g/cm³. Finally, the 5wt% samples recorded an average density of 2.31 ± 0.02 g/cm³, approximately 3% lower than the HAp samples average density (2.38 g/cm³). And it is even lower compared to the theoretical density of HAp (3.17 g/cm³) and the maximum theoretical density of HAp-MgO (3.2 g/cm³).

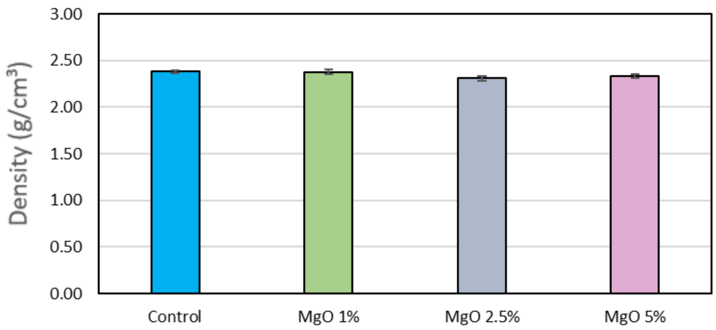

Figure 38 - HAp-MgO Scaffold's density after thermal treatment.

Regarding the porosity of the HAp-MgO scaffolds, an increase is noted in comparison to the control samples (Figure 39). The 1wt% samples exhibit an average total porosity of 60 ± 1.3%, 2% more than the HAp group. Plus, the 2.5wt% and 5wt% MgO composites display even more increasing up to 65 ± 1% (38 ± 1.5% infill porosity and 27% ± 0.7% bulk porosity).

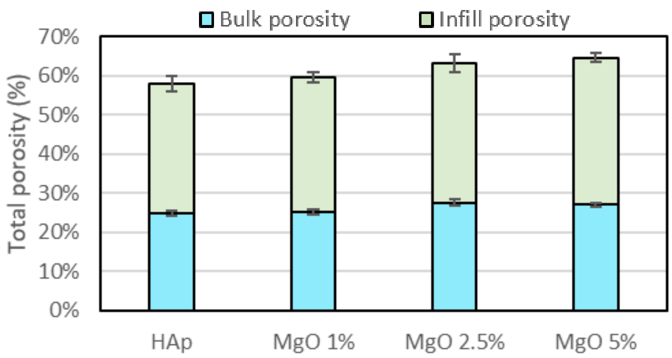

Figure 39 - HAp-MgO Scaffold's Porosity.

6.3. Microstructural analyses

Analyzing the surface morphology of the produced scaffolds through SEM (Figure 40), the HAp-MgO composites appear to be less compact, showing increased porosity between particles. This effect is more evident in the 2.5wt% (Figure 40.C) and 5wt% MgO composite (Figure 40.D). The 1wt% (Figure 40.B) showed some imaging challenges, resulting in lower image quality, but it shows a surface morphology similar to that of the control sample (Figure 40.A).

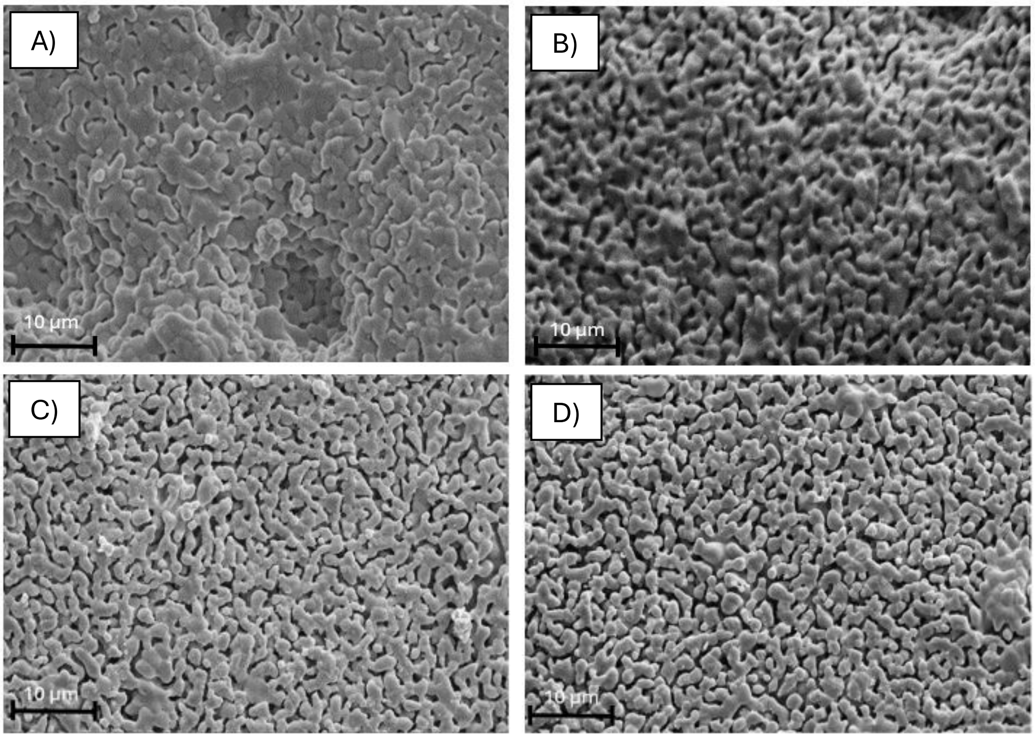

Figure 40 - HAp-MgO Scaffold's SEM at 100x magnification. A) HAp, B) MgO 1%, C) MgO 2.5% e D) MgO 5%.

In the EDS analysis of the 1wt% MgO composite (Figure 41.A), detecting MgO on the surface was challenging due to the quality limitations of the test; a few particle clusters were observed with a very low Mg presence. In the 2.5wt% MgO composite (Figure 41.B), smaller particles than those of HAp were identified, showing a high intensity of Mg and O in these regions, which suggests limited interconnection between HAp and MgO particles. Finally, in the 5wt% MgO composite (Figure 41.C), the increase in porosity is more apparent, with a continued strong presence of MgO particles.

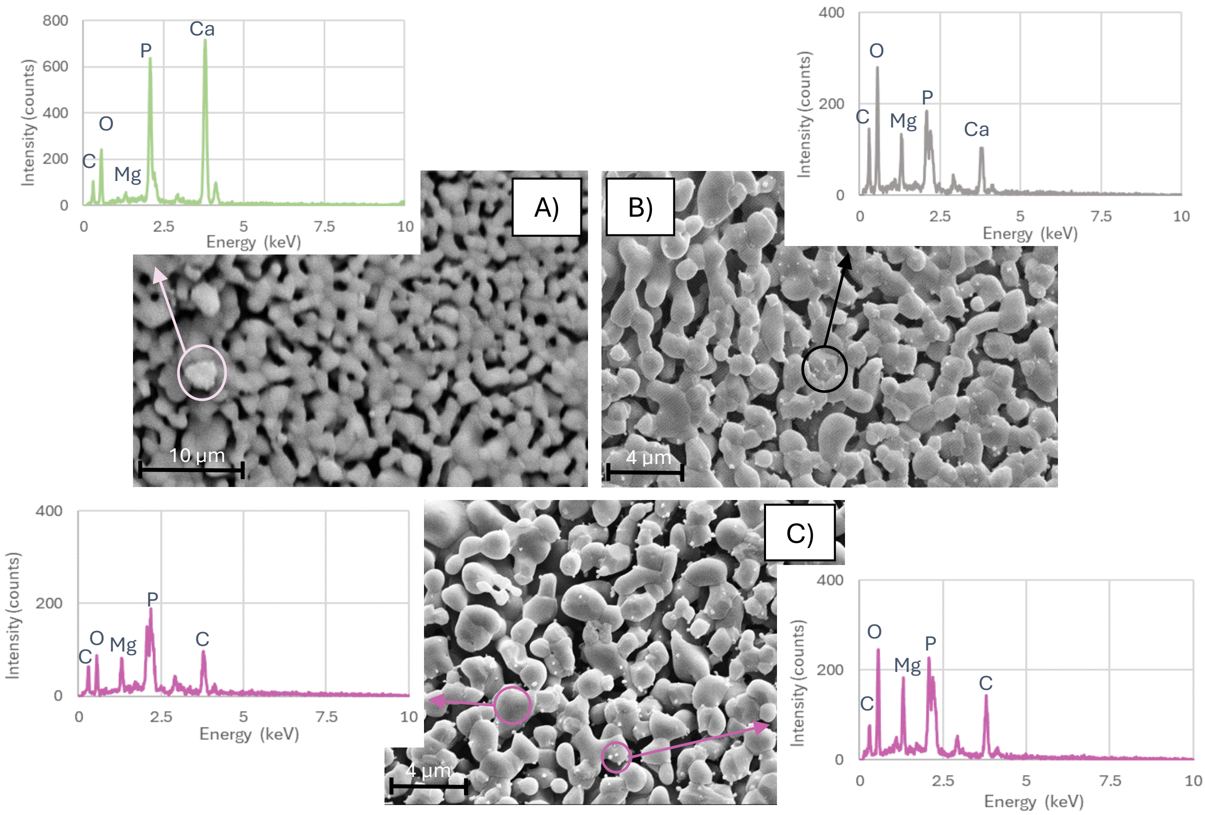

Figure 41 - HAp-MgO Scaffold's SEM/EDS. A) MgO 1%, B) MgO 2.5% and C) MgO 5%.

6.4. Compression test

In the results of the final compression test, the mechanical behavior of scaffolds with increasing percentages of MgO was analyzed. The stress-strain curves (Figure 42.A) indicate an exponential decrease in maximum compressive strength as the amount of MgO increases. The 1wt% MgO composite shows a decline in maximum compression stress values, with the maximum stress of the control sample (HAp) recorded at 15.7 MPa, while the 1wt% composite dropped to 11.8 MPa.

This is further substantiated when comparing the maximum compressive stress values and apparent compressive stiffness recorded for the composites with more MgO (Figure 42.B and 42.C). The 5wt% MgO composites yielded an average value of 5.5 MPa, representing a 65% reduction in maximum stress compared to the HAp samples. Additionally, the apparent compressive stiffness for the 5wt% samples averaged 150 MPa, indicating a 57% decrease compared to the control samples, which had apparent compressive stiffness of 350 MPa. However, the variation values in both the maximum compressive stress and compressive stiffness across the different tests within each group was reduced in the HAp-MgO groups compared to the control group.

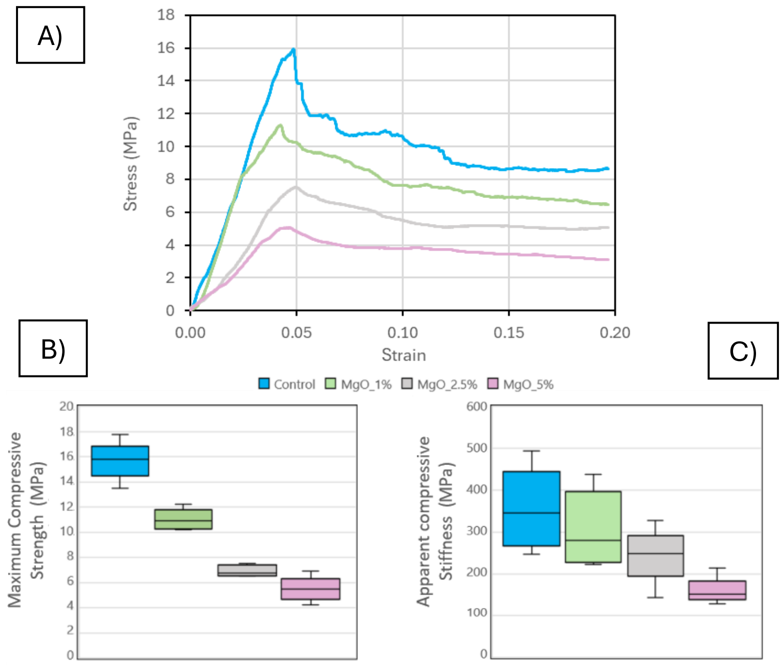

Figure 42 - HAp-MgO Scaffold's compressive Test. A) Compression curve, B) maximum compressive strength and C) Compressive stiffness.

6.5. Degradation test

Analyzing the degradation results of the HAp-MgO samples in PBS (Figure 43), the opposite effect was observed, with all samples recording an increase in weight, particularly those with more concentration. By the end of the experiment, the 2.5wt% and 5wt% MgO group increased to 3.1% and 8.2% of original weight respectively. A higher weight gain was accompanied by a higher standard deviation, due to the higher differences recorded between 5wt% MgO composites. It is important to highlight that in the MgO samples, each time the weight was recorded, or the PBS solution was changed, there were always residual particles, indicating signs of degradation.

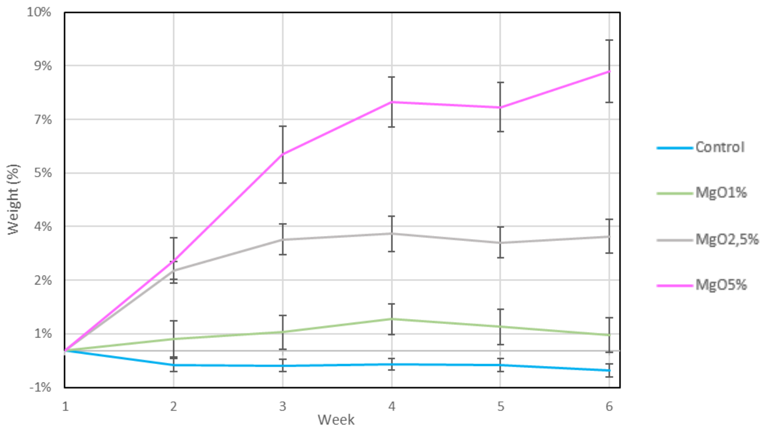

Figure 43 - HAp-MgO Scaffold's degradation test.

The SEM/EDS analysis of the HAp-MgO scaffolds after the degradation test are given in Figure 44. The composites surfaces show morphological change, with a decrease in the microporosity previously noted across all groups. Particle formation is evident on the surfaces of both the 1wt% and 2.5wt% composites. In contrast, the MgO 5% composite that shows significant alterations, with changes apparent across its entire surface.

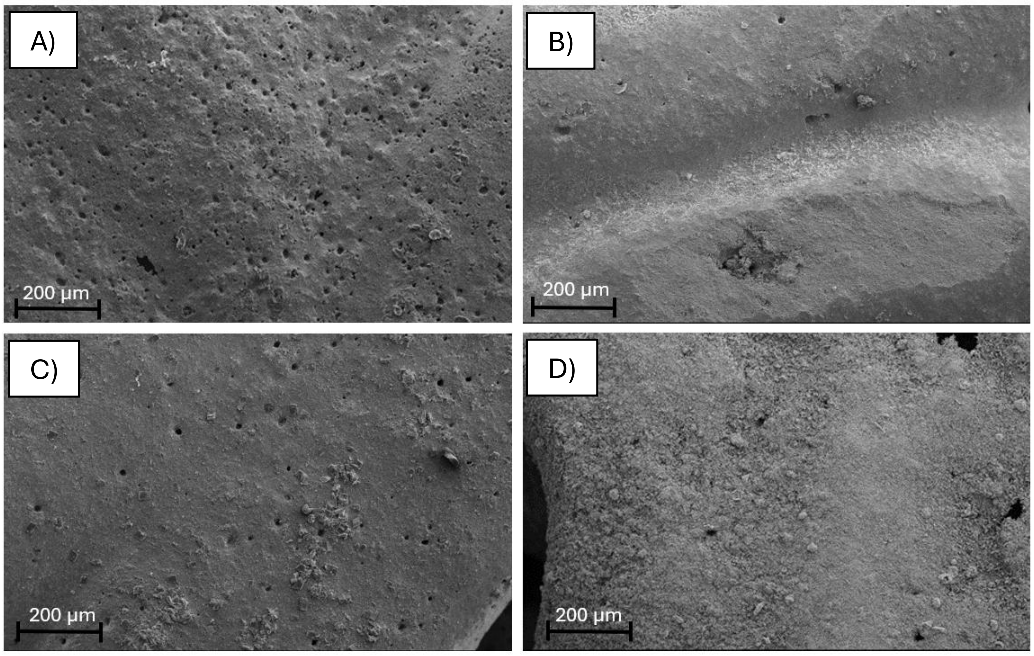

Figure 44 - HAp-MgO Scaffold's SEM analysis after degradation test (100x). A) HAp, B) MgO 1%, C) MgO 2.5% e D) MgO 5%.

Increasing the magnification and conducting the EDS (Figure 45), larger crystals are observed in all samples, with a significant intensity of Mg and O detected, in addition to phosphate and Ca. The MgO 1% (Figure 45.A) is the one with less formation on the surface, but has small Mg particles present, similar to those found in the samples with more concentration before the degradation test. Regarding the MgO 2.5% (Figure 45.B), its surface is largely covered by magnesium phosphate crystals, showing a low quantity of Ca in those regions. Furthermore, in surface areas that are visually closer to the control sample, Mg still is detected in low quantities. Finally, in the MgO 5% (Figure 45.C), its surface is completely modified, with Mg and phosphate detected throughout. This sample exhibits apparent chemical changes with a high reduction in the amount of Ca across the entire region.

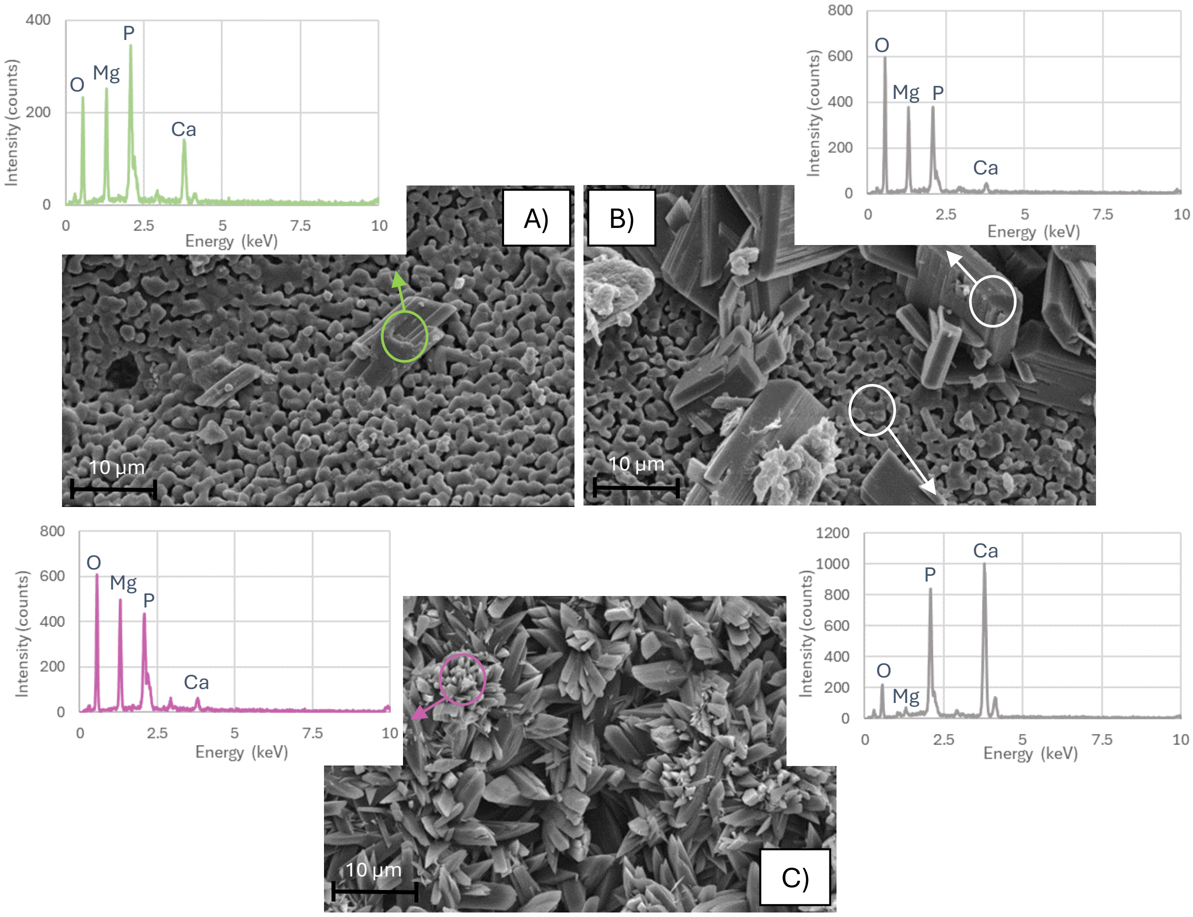

Figure 45 - HAp-MgO Scaffold's SEM/EDS after degradation test (2000x). A) MgO 1%, B) MgO 2.5% and C) MgO 5%.

6.6. Discussion of the incorporation of MgO

Analyzing the rheology of the HAp-MgO pastes (Figure 35) and comparing it with the particle analysis (Figure 9), it was expected that Mg would decrease the viscosity due to its smaller particle size. However, MgO did not dissolve completely in the Darvan solution, settling at the bottom over time if not stirred. As a result, even with the addition of other materials later, the MgO did not properly integrate with the paste. This is confirmed by the SEM analysis, where MgO particles are observed dispersed throughout the HAp-MgO samples. Consequently, the samples with higher MgO content showed an increase in viscosity rather than a decrease, as highlighted in the 5 wt% sample.

Using SEM/EDS (Figure 40 and 41), it is possible to observe that as the amount of MgO increases, the size of the micropores on the surface of the scaffolds also increases. This can be explained by the sintering temperature of MgO, which ranges between 1400 - 1600°C [63], [64]. This leads to a lack of bonding between the HAp and MgO particles during sintering, resulting in numerous MgO particles being scattered throughout the scaffold and causing incomplete sintering.

According to these results, they contribute to the analysis of dimensional and weight loss, as they are related to the sintering of the samples. With more MgO, the composites have higher porosity, which is confirmed both by the SEM and by the calculations made to determine the porosity of the samples. This leads to a consequent loss in density, causing the dimensional loss to be lower than the control sample, while also resulting in a greater weight loss.

Through the compression tests (Figure 42), the HAp-MgO composites show a loss in mechanical strength as the amount of MgO incorporated increases. The sample's maximum stress decreases up to 65% and the apparent compressive stiffness decreases up tp 58% when compared to HAp scaffolds properties. This directly affects the mechanical properties of the composites, which are still similar to the compression properties of trabecular bone, but closer to its minimum value [2]. This outcome is surprising when compared to studies such as those by Xu et al. and Shao H. et al., where the addition of MgO to scaffolds results in an increase in mechanical resistance of the scaffolds. And even in the study by Shao H. et al., the production was done using the same sintering temperature of 1150°C [65], [66].

Analyzing the degradation test (Figure 43), the HAp-MgO samples all showed an increase in weight throughout the test, with the MgO 5% group achieving a weight gain of up to 9%. The HAp-MgO samples analyzed using SEM/EDS (Figure 44 and 45), a formation of crystals on the surface of all the composites was observed. This was most noticeable in the scaffolds with higher concentrations, where the surface was completely altered. One factor indicating the weight gain is the porosity, which decreased in comparison to the samples in Figure 40 that were not in contact with PBS and showed an increase in porosity compared to the control sample. Another factor linking the reduction in porosity with the simultaneous weight gain is the decrease in Ca and the increase in P observed in the EDS analysis. This suggests that the Mg2+ will react with PO2- forming magnesium phosphate that crystallizes on the surface, while Ca2+ is released into the solution.

Chapter 7 - Final discussion

Comparing the rheology results between different scaffolds compositions (Table 4), it is evident that the incorporation of ZnO drastically reduces the viscosity of the paste, achieving a 47.6% decrease compared to the HAp paste, while MgO has the opposite effect, increasing the viscosity up to 34.2%. When comparing these values, it was observed that it was possible to print with a paste with an average apparent viscosity of 36.9 Pa.s (MgO 5%), which indicates that it is feasible to print pastes with a higher solid content by adding ZnO. This approach could further consolidate the printed scaffolds and enhance their mechanical properties.

Table 4 - Viscosity of HAp and HAp composites pastes.

Scaffolds	**HAp**	**ZnO 1%**	**ZnO 2.5%**	**ZnO 5%**	**MgO 1%**	**MgO 2.5%**	**MgO 5%**
V̇ (Pa.s)	27.5(±3.5)	22.2(±3)	13.1(±1.5)	14.3(±2.5)	20.7(±3)	29(±3.1)	36.9(±3.6)

Comparing the scaffolds manufacturing, all scaffolds have an infill porosity lower than the 50% choose in the software, that can be explain by the size of the filaments in SEM analysis (Figure 19), where filament have average of 1mm in diameter compared to 0.65mm programmed in the optimization setting of the software. That extra extruding cause the lower infill porosity around all groups (Figure 46). The HAp-MgO composites shows a higher overall porosity compared to other groups (5,5% higher than the HAp group and up to 8,2% compared to the HAp-ZnO groups).

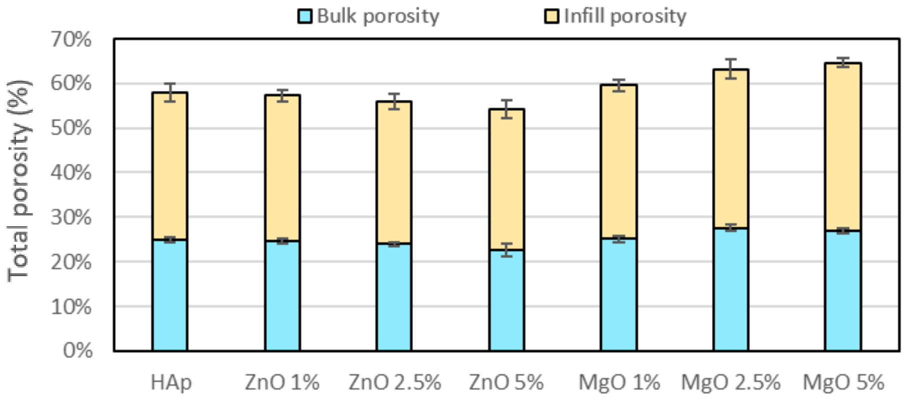

Figure 46 - *HAp and HAp composites porosity.*

This is confirmed by the SEM/EDS analysis, where differences in microporosity between the groups are evident. As seen in Figure 47, compared to the control sample (Figure 47.A), the HAp-MgO sample (Figure 47.C) displays greater microporosity across its entire surface, highlighting sintering issues within this group that prevented the scaffolds from contracting and, as a result, becoming less dense. In contrast, the HAp-ZnO samples achieved better results, surpassing even the control sample.

The SEM/EDS analysis shows that the HAp-MgO scaffolds have MgO particles visibly scattered throughout the surface (Figure 47.C). In contrast, in the HAp-ZnO composites, the presence of Zn is detected across the entire surface, but isolated particles are significantly less frequent (Figure 47.B), due to the lower sintering porosity found in the HAp-ZnO groups.

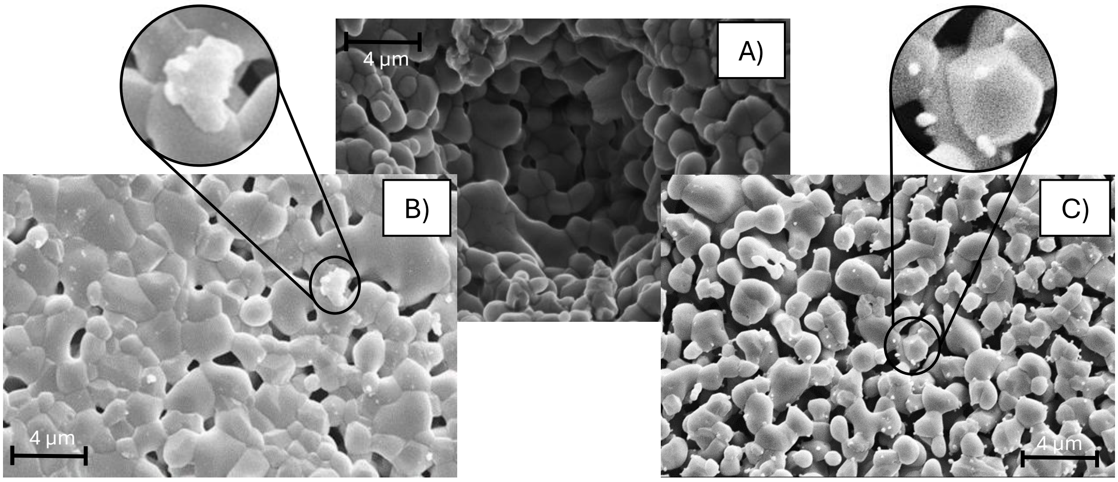

Figure 47 - HAp and HAp composites SEM/EDS (5000x). A) HAp, B) HAp-ZnO 5% and C) HAp-MgO 5%.

This is reflected in the mechanical tests (Table 5), where the HAp-ZnO scaffolds, on average, recorded an average maximum stress 2.8 times higher than the HAp-MgO scaffolds. Specifically, the 5% ZnO sample showed a maximum compressive stress 5.5 times greater than the 5% MgO sample. This demonstrates that the addition of ZnO significantly enhances the mechanical properties of the scaffold.

Table 5 - Scaffolds mechanical properties.

Scaffolds	HAp	ZnO 1%	ZnO 2.5%	ZnO 5%	MgO 1%	MgO 2.5%	MgO 5%
σ_{max} **(MPa)**	15.7 (±1.4)	15.1 (±1.3)	20.6 (±2.5)	33 (±3)	11.8 (±0.7)	7 (±0.5)	5.5 (±1)
E (MPa)	350 (±86)	441 (±134)	605 (±132)	792 (±124)	306 (±91)	244 (±66)	159 (±32)

In the degradation test (Figure 48), it can be observed that each group reacted differently to the presence of PBS. The HAp group (Figure 48.A) appears to be slightly more porous, with less particle bonding compared to the SEM image of the sample before the degradation test (Figure 40.A). This suggests signs of degradation, although not very substantial, as the weight measurement only recorded a 0.6% loss. In the HAp-ZnO composite (Figure 48.B), the formation of, probably, zinc phosphate crystals on the surface of the sample is observed, along with its microporosity in areas without crystals, which is smaller compared to the HAp-ZnO samples without PBS (Figure 40).

The samples without PBS exhibited lower microporosity. On the other hand, the HAp-MgO composite (Figure 48.C) When comparing the groups, it is evident that the HAp-MgO group exhibits the most significant morphological changes, followed by the HAp-ZnO group.

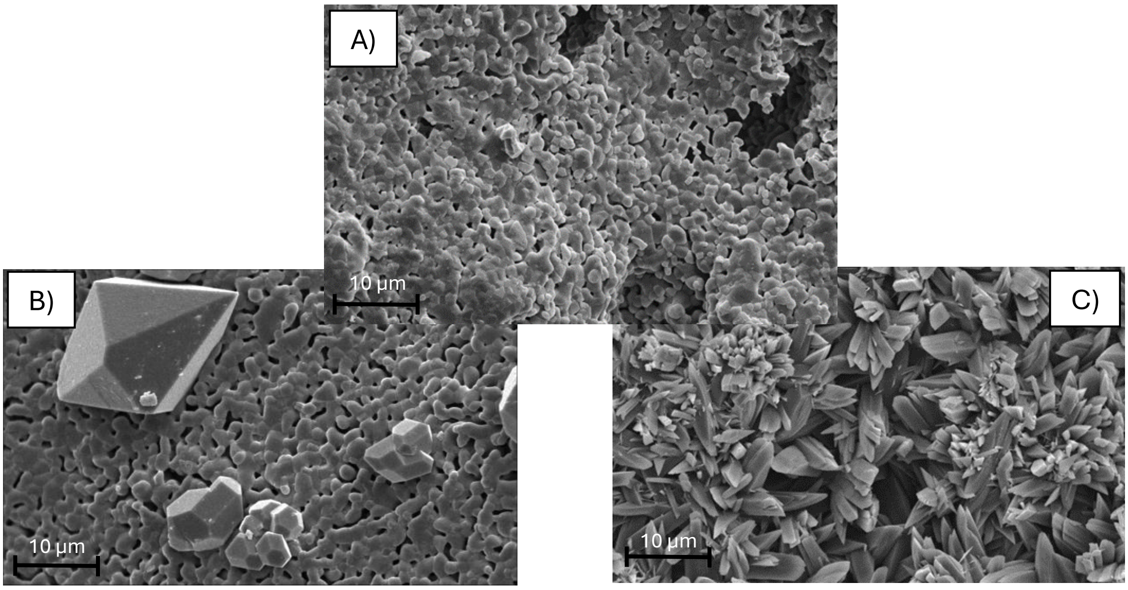

Figure 48 - HAp and HAp composites SEM/EDS after degradation test (2000x). A) HAp, B) HAp-ZnO 5% and C) HAp-MgO 5%.

When comparing the groups, it is evident that the HAp-MgO group exhibits the most significant morphological changes, followed by the HAp-ZnO group. No further tests were conducted on these samples with PBS, making it difficult to determine whether these changes are beneficial or detrimental to bone regeneration.

A common factor observed across all samples is the loss and even gain of weight. It is evident that all samples underwent morphological changes, but there was minimal material release, which could hinder the formation of new bone tissue in these regions. However, it is important to note that this is an *in vitro* test, and it is uncertain whether the samples will behave differently when subjected to *in vivo*.

Chapter 8 - Conclusion and future perspectives

8.1. Conclusion

The main objective of this study was to manufacture scaffolds using Robocasting for bone tissue regeneration. Initially, it was necessary to develop printable pastes and study the printability of different geometries. Additionally, composite scaffolds were made by incorporating ZnO and MgO to improve the base HAp scaffolds properties. To evaluate these properties, comprehensive studies were performed focusing on their morphology, compressive strength, and in vitro degradation behavior in PBS.

The results of this study demonstrate that HAp scaffolds produced via Robocasting were successfully developed, achieving a paste with a solid concentration of 58wt% and an apparent printing viscosity of 27.5 ± 3.5 Pa.s. The findings also highlighted the necessity of additives, particularly Darvan, which significantly reduced viscosity and allowed for the incorporation of higher solid content.

Production and analysis of different geometries observed that the Honeycomb geometry exhibited the best compressive mechanical properties, with 15.7 ± 1.4 MPa maximum compressive strength. Leading to its selection as a model geometry for the HAp-ZnO and HAp-MgO scaffolds.

Using SEM analysis, it was possible to examine the 3 different levels of porosity within the scaffolds. An infill porosity with an average size of 700 μm, and air bubble and sintering porosity with an average of 50 μm and 2 μm respectively. The EDS analysis helps to detect and confirm the presence of ZnO and MgO in the composites, and understanding how these materials influenced the microstructural surface, like lowering the sintering porosity in case of the HAp-ZnO or increasing in HAp-MgO composites.

Compression tests of the HAp composites revealed that each composition exhibited distinct mechanical behavior. Notably, the HAp-ZnO groups demonstrated a significant increase in maximum compressive strength up to 33 ± 3 MPa, even exceeding the average values of trabecular bone.

Moreover, degradation tests showed the low degradation rate of HAp, while the composite scaffolds interacted with PBS, leading to the formation crystals on the samples surfaces probably of zinc phosphate and magnesium phosphate, as well as the release of Ca^{2+} ions. The surface modification and ion release was particularly notable in the HAp-MgO group.

In summary, it was possible to successfully print and produce composite scaffolds using 3D printing, demonstrating the ability to develop complex geometries with suitable rheological properties and compressive strength comparable to trabecular bone. The incorporation of ZnO and MgO alongside HAp showed promising results in these initial tests to produce customizable bone substitutes. However, further studies are necessary to investigate their specific properties, particularly in terms of osteoinduction and antibacterial activity.

8.2. Future perspectives

Even though the main objective of the work has been completed, there is always space for improvements to continue the work forward.

Firstly, it would be valuable to further explore the preparation of the pastes, aiming to increase their solid content and improve their formulation to make the drying process easier to control, thereby reducing the likelihood of cracks.

Another interesting point to consider is the biological tests of the scaffolds, to study their levels of biocompatibility with bone tissue growth. Furthermore, studying how the production of composite scaffolds influences these properties, particularly their antibacterial properties and osteoinduction potential, is essential.

Finally, exploring designs tailored specifically to trauma cases would be highly beneficial. In this study, scaffold production focused on cubic geometries with fixed dimensions. Future research could build upon resolved clinical cases, analyzing how this technique might have provided benefits in those scenarios.

References

[1] C. L. . VanPutte, J. L. . Regan, and A. F. . Russo, *Seeley's essentials of anatomy & physiology*. McGraw-Hill Education, 2016.

[2] A. Wubneh, E. K. Tsekoura, C. Ayranci, and H. Uludağ, "Current state of fabrication technologies and materials for bone tissue engineering," Oct. 15, 2018, *Acta Materialia Inc*. doi: 10.1016/j.actbio.2018.09.031.

[3] Ž. Perić Kačarević *et al.*, "An introduction to bone tissue engineering," Feb. 01, 2020, *SAGE Publications Ltd*. doi: 10.1177/0391398819876286.

[4] J. S. Kenkre and J. H. D. Bassett, "The bone remodelling cycle," May 01, 2018, *SAGE Publications Ltd*. doi: 10.1177/0004563218759371.

[5] J. O. Gordeladze, H. J. Haugen, S. P. Lyngstadaas, and J. E. Reseland, "6 Bone Tissue Engineering: State of the Art, Challenges, and Prospects," 2017.

[6] A. Salhotra, H. N. Shah, B. Levi, and M. T. Longaker, "Mechanisms of bone development and repair," Nov. 01, 2020, *Nature Research*. doi: 10.1038/s41580-020-00279-w.

[7] A. D. Bagde *et al.*, "State of the Art Technology for Bone Tissue Engineering and Drug Delivery," Jun. 01, 2019, *Elsevier Masson SAS*. doi: 10.1016/j.irbm.2019.03.001.

[8] L. Roseti *et al.*, "Scaffolds for Bone Tissue Engineering: State of the art and new perspectives," Sep. 01, 2017, *Elsevier Ltd*. doi: 10.1016/j.msec.2017.05.017.

[9] T. Genova, I. Roato, M. Carossa, C. Motta, D. Cavagnetto, and F. Mussano, "Advances on bone substitutes through 3d bioprinting," Oct. 01, 2020, *MDPI AG*. doi: 10.3390/ijms21197012.

[10] T. Ghassemi, A. Shahroodi, M. H. Ebrahimzadeh, A. Mousavian, J. Movaffagh, and A. Moradi, "CURRENT CONCEPTS REVIEW Current Concepts in Scaffolding for Bone Tissue Engineering," 2018. [Online]. Available: http://abjs.mums.ac.irtheonlineversionofthisarticleabjs.mums.ac.ir

[11] A. Marques, G. Miranda, F. Silva, P. Pinto, and Ó. Carvalho, "Review on current limits and potentialities of technologies for biomedical ceramic scaffolds production," Mar. 01, 2021, *John Wiley and Sons Inc*. doi: 10.1002/jbm.b.34706.

[12] N. Abbasi, S. Hamlet, R. M. Love, and N. T. Nguyen, "Porous scaffolds for bone regeneration," Mar. 01, 2020, *Elsevier B.V.* doi: 10.1016/j.jsamd.2020.01.007.

[13] S. Kalsi, J. Singh, S. S. Sehgal, and N. K. Sharma, "Biomaterials for tissue engineered bone Scaffolds: A review," in *Materials Today: Proceedings*, Elsevier Ltd, 2021, pp. 888–893. doi: 10.1016/j.matpr.2021.04.273.

[14] H. Qu, H. Fu, Z. Han, and Y. Sun, "Biomaterials for bone tissue engineering scaffolds: a review," 2019, doi: 10.1039/c9ra05214c.

[15] E. Cunningham, N. Dunne, G. Walker, C. Maggs, R. Wilcox, and F. Buchanan, "Hydroxyapatite bone substitutes developed via replication of natural marine sponges," *J Mater Sci Mater Med*, vol. 21, no. 8, pp. 2255–2261, Aug. 2010, doi: 10.1007/s10856-009-3961-4.

[16] "Bioceramed | Portugal." Accessed: Oct. 20, 2024. [Online]. Available: https://www.bioceramed.com/

[17] L. Figueiredo, R. Fonseca, L. F. V. Pinto, F. C. Ferreira, A. Almeida, and A. Rodrigues, "Strategy to improve the mechanical properties of bioabsorbable materials based on chitosan for orthopedic fixation applications," *J Mech Behav Biomed Mater*, vol. 103, Mar. 2020, doi: 10.1016/j.jmbbm.2019.103572.

[18] R. Trombetta, J. A. Inzana, E. M. Schwarz, S. L. Kates, and H. A. Awad, "3D Printing of Calcium Phosphate Ceramics for Bone Tissue Engineering and Drug Delivery," *Ann Biomed Eng*, vol. 45, no. 1, pp. 23–44, Jan. 2017, doi: 10.1007/s10439-016-1678-3.

[19] J. Lai, C. Wang, and M. Wang, "3D printing in biomedical engineering: Processes, materials, and applications," Jun. 01, 2021, *American Institute of Physics Inc.* doi: 10.1063/5.0024177.

[20] V. M. Vaz and L. Kumar, "3D Printing as a Promising Tool in Personalized Medicine," Jan. 01, 2021, *Springer Science and Business Media Deutschland GmbH*. doi: 10.1208/s12249-020-01905-8.

[21] P. Feng, J. Jia, M. Liu, S. Peng, Z. Zhao, and C. Shuai, "Degradation mechanisms and acceleration strategies of poly (lactic acid) scaffold for bone regeneration," *Mater Des*, vol. 210, Nov. 2021, doi: 10.1016/j.matdes.2021.110066.

[22] Y. Chen, W. Li, C. Zhang, Z. Wu, and J. Liu, "Recent Developments of Biomaterials for Additive Manufacturing of Bone Scaffolds," Dec. 01, 2020, *Wiley-VCH Verlag*. doi: 10.1002/adhm.202000724.

[23] S. Lamnini, H. Elsayed, Y. Lakhdar, F. Baino, F. Smeacetto, and E. Bernardo, "Robocasting of advanced ceramics: ink optimization and protocol to predict the printing parameters - A review," Sep. 01, 2022, *Elsevier Ltd*. doi: 10.1016/j.heliyon.2022.e10651.

[24] V. Saggiomo, "3D printed devices for catalytic systems," in *Catalyst Immobilization: Methods and Applications*, wiley, 2019, pp. 369–408. doi: 10.1002/9783527817290.ch11.

[25] E. Peng, D. Zhang, and J. Ding, "Ceramic Robocasting: Recent Achievements, Potential, and Future Developments," Nov. 22, 2018, *Wiley-VCH Verlag*. doi: 10.1002/adma.201802404.

[26] M. H. Monfared *et al.*, "A deep insight into the preparation of ceramic bone scaffolds utilizing robocasting technique," Mar. 01, 2022, *Elsevier Ltd*. doi: 10.1016/j.ceramint.2021.11.268.

[27] E. Feilden, "Additive Manufacturing of Ceramics and Ceramic Composites via Robocasting," Imperial College London, 2017. Accessed: Nov. 05, 2024. [Online]. Available: https://core.ac.uk/download/pdf/146459525.pdf

[28] V. Minerals, "VANDERBILT Minerals Technical Data DARVAN ® 811 Dispersing Agent Sodium Polyacrylate for Ceramic Bodies and Glazes," Oct. 2014 Accessed: Nov. 02, 2024. [Online]. Available: https://www.vanderbiltminerals.com/resources/TDS_DARVAN_811_C_and_R_Web.pdf

[29] G. Montalbano, G. Molino, S. Fiorilli, and C. Vitale-Brovarone, “Synthesis and incorporation of rod-like nano-hydroxyapatite into type I collagen matrix: A hybrid formulation for 3D printing of bone scaffolds,” *J Eur Ceram Soc*, vol. 40, no. 11, pp. 3689–3697, Sep. 2020, doi: 10.1016/j.jeurceramsoc.2020.02.018.

[30] M. Teodorescu, M. Bercea, and S. Morariu, “Biomaterials of PVA and PVP in medical and pharmaceutical applications: Perspectives and challenges,” Jan. 01, 2019, *Elsevier Inc.* doi: 10.1016/j.biotechadv.2018.11.008.

[31] A. Kumar and S. S. Han, “PVA-based hydrogels for tissue engineering: A review,” Mar. 04, 2017, *Taylor and Francis Inc.* doi: 10.1080/00914037.2016.1190930.

[32] W. Zhang, J. Chen, Q. Chen, H. Wu, and W. Mu, “Sugar alcohols derived from lactose: lactitol, galactitol, and sorbitol”, doi: 10.1007/s00253-020-10929-w/Published.

[33] L. S. Ribeiro, J. J. M. Órfão, and M. F. R. Pereira, “Comparative study of different catalysts for the direct conversion of cellulose to sorbitol,” *Green Processing and Synthesis*, vol. 4, no. 2, pp. 71–78, Apr. 2015, doi: 10.1515/gps-2014-0091.

[34] S. Roulon *et al.*, “D-sorbitol physical properties effects on filaments used by 3d printing process for personalized medicine,” *Molecules*, vol. 26, no. 10, May 2021, doi: 10.3390/molecules26103000.

[35] G. Falcone, S. Kuth, A. R. Boccaccini, R. P. Aquino, T. Esposito, and P. Russo, “Application of Calcium Alginate Hydrogels in Semisolid Extrusion 3D Printed for the Production of Easy-to-Swallow Tablets,” *Adv Eng Mater*, vol. 25, no. 9, May 2023, doi: 10.1002/adem.202201476.

[36] H. Shi, Z. Zhou, W. Li, Y. Fan, Z. Li, and J. Wei, “Hydroxyapatite based materials for bone tissue engineering: A brief and comprehensive introduction,” Jan. 01, 2021, *MDPI AG*. doi: 10.3390/cryst11020149.

[37] S. Panda, C. K. Biswas, and S. Paul, “A comprehensive review on the preparation and application of calcium hydroxyapatite: A special focus on atomic doping methods for bone tissue engineering,” Oct. 15, 2021, *Elsevier Ltd*. doi: 10.1016/j.ceramint.2021.07.100.

[38] G. L. Darimont, R. Cloots, E. Heinen, L. Seidel, and R. Legrand, “In vivo behaviour of hydroxyapatite coatings on titanium implants: a quantitative study in the rabbit,” 2002.

[39] I. Ielo, G. Calabrese, G. De Luca, and S. Conoci, “Recent Advances in Hydroxyapatite-Based Biocomposites for Bone Tissue Regeneration in Orthopedics,” Sep. 01, 2022, *MDPI*. doi: 10.3390/ijms23179721.

[40] M. Sartori *et al.*, “Long-term in vivo experimental investigations on magnesium doped hydroxyapatite bone substitutes,” *J Mater Sci Mater Med*, vol. 25, no. 6, pp. 1495–1504, Jun. 2014, doi: 10.1007/s10856-014-5177-5.

[41] S. Kumar, C. Gautam, B. S. Chauhan, S. Srikrishna, R. S. Yadav, and S. B. Rai, “Enhanced mechanical properties and hydrophilic behavior of magnesium oxide added hydroxyapatite nanocomposite: A bone substitute material for load bearing applications,” *Ceram Int*, vol. 46, no. 10, pp. 16235–16248, Jul. 2020, doi: 10.1016/j.ceramint.2020.03.180.

[42] D. J. Hickey, B. Ercan, L. Sun, and T. J. Webster, “Adding MgO nanoparticles to hydroxyapatite-PLLA nanocomposites for improved bone tissue engineering applications,” *Acta Biomater*, vol. 14, pp. 175–184, Mar. 2015, doi: 10.1016/j.actbio.2014.12.004.

[43] Z. Chen, W. Zhang, M. Wang, L. J. Backman, and J. Chen, “Effects of Zinc, Magnesium, and Iron Ions on Bone Tissue Engineering,” Jun. 13, 2022, *American Chemical Society*. doi: 10.1021/acsbiomaterials.2c00368.

[44] P. Zhu *et al.*, “Biomedical Applications of Functionalized ZnO Nanomaterials: From Biosensors to Bioimaging,” Jan. 07, 2016, *Wiley-VCH Verlag*. doi: 10.1002/admi.201500494.

[45] V. Saxena, A. Hasan, and L. M. Pandey, “Effect of Zn/ZnO integration with hydroxyapatite: a review,” *Materials Technology*, vol. 33, no. 2, pp. 79–92, Jan. 2018, doi: 10.1080/10667857.2017.1377972.

[46] I. Uysal, B. Yilmaz, and Z. Evis, “Zn-doped hydroxyapatite in biomedical applications”, doi: 10.1007/s41779-021-00583-4/Published.

[47] P. Feng, P. Wei, C. Shuai, and S. Peng, “Characterization of mechanical and biological properties of 3-D scaffolds reinforced with zinc oxide for bone tissue engineering,” *PLoS One*, vol. 9, no. 1, Jan. 2014, doi: 10.1371/journal.pone.0087755.

[48] A. V. Girão, G. Caputo, and M. C. Ferro, “Application of Scanning Electron Microscopy–Energy Dispersive X-Ray Spectroscopy (SEM-EDS),” *Comprehensive Analytical Chemistry*, vol. 75, pp. 153–168, 2017, doi: 10.1016/bs.coac.2016.10.002.

[49] Z. P. Tshabalala, D. N. Oosthuizen, H. C. Swart, and D. E. Motaung, “Tools and techniques for characterization and evaluation of nanosensors,” in *Nanosensors for Smart Cities*, Elsevier, 2020, pp. 85–110. doi: 10.1016/B978-0-12-819870-4.00005-0.

[50] S. Kanwar and S. Vijayavenkataraman, “Design of 3D printed scaffolds for bone tissue engineering: A review,” Dec. 01, 2021, *Elsevier B.V.* doi: 10.1016/j.bprint.2021.e00167.

[51] H. Shao, J. He, T. Lin, Z. Zhang, Y. Zhang, and S. Liu, “3D gel-printing of hydroxyapatite scaffold for bone tissue engineering,” *Ceram Int*, vol. 45, no. 1, pp. 1163–1170, Jan. 2019, doi: 10.1016/j.ceramint.2018.09.300.

[52] D. X. B. Chen, *Extrusion Bioprinting of Scaffolds for Tissue Engineering Applications*. Springer, 2019. doi: https://doi.org/10.1007/978-3-030-03460-3.

[53] C. OKYAY and B. SAĞBAŞ, “Determining optimal robocasting process parameters for additive manufacturing of ceramic parts,” *International Journal of 3D Printing Technologies and Digital Industry*, vol. 5, no. 3, pp. 435–444, Dec. 2021, doi: 10.46519/ij3dptdi.904697.

[54] H. Mohammadi, M. Sepantafar, N. Muhamad, and A. Bakar Sulong, “How Does Scaffold Porosity Conduct Bone Tissue Regeneration?,” Oct. 01, 2021, *John Wiley and Sons Inc*. doi: 10.1002/adem.202100463.

[55] M. Trzaskowska, V. Vivcharenko, and A. Przekora, “The Impact of Hydroxyapatite Sintering Temperature on Its Microstructural, Mechanical, and Biological Properties,” Mar. 01, 2023, *Multidisciplinary Digital Publishing Institute (MDPI)*. doi: 10.3390/ijms24065083.

[56] G. Muralithran and S. Ramesh, "The effects of sintering temperature on the properties of hydroxyapatite," Mar. 2000. doi: https://doi.org/10.1016/S0272-8842(99)00046-2.

[57] S. Wang *et al.*, "Honeycomb structure is promising for the repair of human bone defects," *Mater Des*, vol. 207, Sep. 2021, doi: 10.1016/j.matdes.2021.109832.

[58] F. Scocozza, G. M. Di Gravina, E. Bari, F. Auricchio, M. L. Torre, and M. Conti, "Prediction of the mechanical response of a 3D (bio)printed hybrid scaffold for improving bone tissue regeneration by structural finite element analysis," *J Mech Behav Biomed Mater*, vol. 142, Jun. 2023, doi: 10.1016/j.jmbbm.2023.105822.

[59] R. L. Reyes, M. S. Ghim, N. U. Kang, J. W. Park, S. J. Gwak, and Y. S. Cho, "Development and assessment of modified-honeycomb-structure scaffold for bone tissue engineering," *Addit Manuf*, vol. 54, Jun. 2022, doi: 10.1016/j.addma.2022.102740.

[60] H. Shao *et al.*, "Bioactive glass-reinforced bioceramic ink writing scaffolds: Sintering, microstructure and mechanical behavior," *Biofabrication*, vol. 7, no. 3, Sep. 2015, doi: 10.1088/1758-5090/7/3/035010.

[61] A. Naqshbandi, I. Sopyan, Gunawan, and Suryanto, "Sol-gel synthesis of Zn doped HA powders and their conversion to porous bodies," in *Applied Mechanics and Materials*, 2014, pp. 603–608. doi: 10.4028/www.scientific.net/AMM.493.603.

[62] M. Mazaheri, A. M. Zahedi, and S. K. Sadrnezhaad, "Two-step sintering of nanocrystalline ZnO compacts: Effect of temperature on densification and grain growth," *Journal of the American Ceramic Society*, vol. 91, no. 1, pp. 56–63, Jan. 2008, doi: 10.1111/j.1551-2916.2007.02029.x.

[63] D. Chen, E. H. Jordan, and M. Gell, "Pressureless sintering of translucent MgO ceramics," *Scr Mater*, vol. 59, no. 7, pp. 757–759, Oct. 2008, doi: 10.1016/j.scriptamat.2008.06.007.

[64] T. K. Gupta, "Sintering of MgO: Densification and Grain Growth," 1971. doi: https://doi.org/10.1007/BF00550287.

[65] D. Xu, Z. Xu, L. Cheng, X. Gao, J. Sun, and L. Chen, "Improvement of the mechanical properties and osteogenic activity of 3D-printed polylactic acid porous scaffolds by nano-hydroxyapatite and nano-magnesium oxide," *Heliyon*, vol. 8, no. 6, Jun. 2022, doi: 10.1016/j.heliyon.2022.e09748.

[66] H. Shao *et al.*, "3D robocasting magnesium-doped wollastonite/TCP bioceramic scaffolds with improved bone regeneration capacity in critical sized calvarial defects," *J Mater Chem B*, vol. 5, no. 16, pp. 2941–2951, 2017, doi: 10.1039/c7tb00217c.